Numerical simulation of buckling and asymmetric behavior of flexible filament using temporal second-order immersed boundary method

Received 9 June 2019
Revised 19 July 2019
Accepted 30 July 2019

Mithun Kanchan and Ranjith Maniyeri
Department of Mechanical Engineering, National Institute of Technology, Surathkal, India

Abstract

Purpose – The purpose of this paper is to perform two-dimensional numerical simulation involving fluid-structure interaction of flexible filament. The filament is tethered to the bottom of a rectangular channel with oscillating fluid flow inlet conditions at low Reynolds number. The simulations are performed using a temporal second-order finite volume-based immersed boundary method (IBM). Further, to understand the relation between different aspect ratios i.e. ratio of filament length to channel height (Len/H) and fixed channel geometry ratio, i.e. ratio of channel height to channel length (H/Lc) on mixing and pumping capabilities.

Design/methodology/approach – The discretization of governing continuity and Navier–Stokes equation is done by finite-volume method on a staggered Cartesian grid. SIMPLE algorithm is used to solve fluid velocity and pressure terms. Two cases of oscillatory flow conditions are used with the flexible filament tethered at the center of bottom channel wall. The first case is sinusoidal oscillatory flow with phase shift (SOFPS) and second case is sinusoidal oscillatory flow without phase shift (SOF). The simulation results are validated with filament dynamics studies of previous researchers. Further, parametric analysis is carried to study the effect of filament length (aspect ratio), filament bending rigidity and Reynolds number on the complex deformation and behavior of flexible filament interacting with nearby oscillating fluid motion.

Findings – It is found that selection of right filament length and bending rigidity is crucial for fluid mixing scenarios. The phase shift in fluid motion is also found to critically effect filament displacement dynamics, especially for rigid filaments. Aspect ratio, suitable for mixing applications is dependent on channel geometry ratio. Symmetric deformation is observed for filaments subjected to SOFPS condition irrespective of bending rigidity, whereas medium and low rigidity filaments placed in SOF condition show severe asymmetric behavior. Two key findings of this study are: symmetric filament conformity without appreciable bending produces sweeping motion in fluid flow, which is highly suited for mixing application; and asymmetric behavior shown by the filament depicts antiplectic metachronism commonly found in beating cilia. As a result, it is possible to pin point the type of fluid motion governing fluid mixing and fluid pumping. The developed computational model can, thus, successfully demonstrate filament-fluid interaction for a wide variety of similar problems.

Originality/value – The present study uses a temporal second-order finite volume-based IBM to examine flexible filament dynamics for various applications such as fluid mixing. Also, it highlights the relationship between channel geometry ratio and filament aspect ratio and its effect on filament sweep patterns. The study

This research was supported by Science and Engineering Research Board, a statutory body of Department of Science and Technology (DST), Government of India through the funded project ECR/2016/001501.

International Journal of Numerical Methods for Heat & Fluid Flow
Vol. 30 No. 3, 2020
pp. 1047-1095

0961-5539
DOI 10.1108/HFF-06-2019-0467

further reports the effect of filament displacement dynamics with or without phase shift for inlet oscillating fluid flow condition.

Keywords Finite volume method, Immersed boundary method, Flexible filament, Low Reynolds number, SIMPLE algorithm

Paper type Research paper

Nomenclature

$\mathbf{x}$ = Dimensionless position vector of fluid grid (Eulerian);
$\mathbf{X}$ = Dimensionless position vector of IB points (Lagrangian);
s = Lagrangian material point;
L_{ref} = Characteristic length scale;
u_{ref} = Characteristic velocity scale;
$\mathbf{u(x,t)}$ = Dimensionless fluid velocity;
$\mathbf{U(s,t)}$ = Dimensionless Lagrangian velocity;
p = Dimensionless fluid pressure;
t = Dimensionless time;
n = initial time level;
$\mathbf{f(x,t)}$ = Dimensionless momentum forcing term;
$\mathbf{F(s,t)}$ = Dimensionless Lagrangian forcing term;
T_{elas} = Filament stretching co-efficient;
S_{ben} = Filament bending stiffness;
H = Dimensionless height of channel;
Len = Dimensionless length of filament;
Len/H = Filament aspect ratio;
Lc = Dimensionless length of channel;
H/Lc = Channel geometry ratio;
Re = Reynolds number;
St = Strouhal number;
f = frequency of oscillation; and
d_{ee} = Filament end-to-end distance.

Greek symbols

ρ = Fluid density;
μ = Fluid viscosity;
δ (x-X) = Discrete dirac delta function;
ε = Filament length error;
Θ = Angle made by the filament with respect to horizontal plane; and
Φ = Probability distribution of time spent by filament at various angles.

Superscripts

* = Dimensional

1. Introduction

The interaction between flexible filament and fluid are encountered in a wide range of natural and industrial scenarios. Some examples in biology include microtubules and F-actin biopolymer cells, red blood cell conformation, opening and closing of the heart valve leaflet, cilia and flagella of micro-organism, DNA strand, cellulose fiber bundling, etc. The filament

often exists in a fluid medium, and thus, a two-way coupled interaction is formed between flexible structure and flowing fluid. In many of the two-way fluid-structure interaction problems, forces generated from both solid and fluid have a tremendous influence on the resulting motion of each other, and hence, cannot be neglected. When a passive flexible filament interacts with fluid, the structure forcefully adheres to the dynamics of the surrounding fluid flow and undergoes deformation accordingly. In return, the fluid produces hydrodynamic stresses on the filament. This combined interactive effect can produce stretching/compression and bending of the body. A crucial factor that governs this behavior of filament to such complex interactions is flexibility (bending rigidity) and length.

Many studies have been carried out in the field of dynamics of flexible filament motion, which includes flapping filament and flag problem (Connell and Yue, 2007; Huang *et al.*, 2007; Xia and Lin, 2008; Huang and Sung, 2010; Ryu *et al.*, 2018), filament motion in soap film (Zhu and Peskin, 2002; Farnell *et al.*, 2004), valve motion in channel (Baaijens, 2001; Yu, 2005) and actuated cilia motion (Alexeev *et al.*, 2008; Dauptain *et al.*, 2008). Specific applications related to flapping filament dynamics in biomimetics involve fluid pumping and fluid mixing. In this direction, Khatavkar *et al.* (2007) had analyzed active micro mixers based on cilia propulsion. By generating a proper scheme of actuation, two filament actuators placed on the same side of the channel wall can produce chaotic mixing in an effective manner. The aspect ratio i.e. the ratio of filament length to channel height (Len/H) in their study was taken between 0.2-0.4 and channel geometry ratio i.e. the ratio of channel height to channel length (H/Lc) was taken as 0.1667. In another work, Lambert and Rangel (2010) studied the effect of filament flap deformation on fluid mixing. They demonstrated that an aspect ratio of 0.667 can produce optimum mixing. Further, they observed that a single filament can also produce rapid mixing in an enhanced manner as compared to multiple flaps. However, the channel geometry ratio in their work was 0.48. Now, let us focus on the various techniques used to simulate the filament dynamics.

The equations governing filament flapping in variety of flow conditions have been solved using analytical and numerical methods. Based on the differential treatment of fluid-solid interfaces, various numerical techniques have been developed. For example, in Arbitrary Lagrange–Eulerian (ALE) (Hu *et al.*, 2001) method no-slip boundary conditions at the interface are applied directly and there is no overlap between solid and fluid domains. However, the computational challenge arises when boundary conditions are to be satisfied directly. To track the changing position of solid and fluid interface, an updating of fluid mesh is required at each time step. Such re-meshing techniques applied in ALE makes it quite impractical for moving mesh and large distortion problems. Also, the per-grid-point operation cost increases drastically. There are other numerical methods such as fictitious-domain method (DLM), smooth particle hydrodynamics (SPH) (Li *et al.*, 2018), lattice Boltzmann method (LBM) and immersed boundary method (IBM) that avoid grid conformation and provide better fluid-structure coupling capabilities. Combined strategies involving IB-LBM have also been extensively studied for fluid and thermal problems (Adeeb *et al.*, 2018; Bamiro and Liou, 2013). DLM and LBM were initially developed for fluid-structure interaction problems involving rigid bodies (Ladd, 1994; Krafczyk *et al.*, 2001; Lallemand and Luo, 2003; Diaz-Goano *et al.*, 2003; Ardekani *et al.*, 2008) while IBM could handle thin elastic structures such as membranes and filaments.

The IBM (Peskin, 1972) is a mathematical framework initially developed by Peskin (2002) to simulate two-way coupling and capture the interaction between thin deformable structure and surrounding fluid. The method was originally created to model a functioning human heart and also to study dynamics of heart wall leaflets (Griffith *et al.*, 2009). Over the years, IBM has proved to be an effective scheme for solving many other complex bio fluid

dynamics problems such as cell and capsule deformation (Rejniak and Dillon, 2007; Huang *et al.*, 2012; Shin and Sung, 2012; Kim *et al.*, 2015), locomotion of jellyfish (Huang and Sung, 2009; Park *et al.*, 2014; Park *et al.*, 2015), flagellum of bacteria (Qin *et al.*, 2012; Maniyeri *et al.*, 2012; Maniyeri and Kang, 2014a, 2014b), two- and three-dimensional parachute aerodynamics (Kim and Peskin, 2006; Kim and Peskin, 2009), droplet dynamics in shear flow (Hua *et al.*, 2014), valveless pumping (Shin and Sung, 2010; Shin *et al.*, 2012), flexible propulsor and fins (Kim *et al.*, 2016; Kim *et al.*, 2017), multiphase flow (Francois *et al.*, 2004), immersed heat transfer (Shu *et al.*, 2013; De Marinis *et al.*, 2016; Santarelli *et al.*, 2016), etc. IBM uses boundary surface regularization approach. The fluid domain, on one hand, is discretized using Eulerian grids while on the other the immersed boundary is discretized by moving Lagrangian grid points, also called IB points. The traction jump across the immersed boundary is modified into body force, which gets distributed onto the fluid volumetric mesh in vicinity of boundary. Thus, to account for the presence of structure and to impose no-slip boundary condition, a momentum forcing term is added to the Navier–Stokes equation. To smoothen the sharp interface caused by the presence of solid structure, a distribution function called Dirac delta function is incorporated. No form of discontinuity arises in solution across the immersed surface. This technique is also referred to as continuous forcing approach. Irrespective of the shape and geometric features of the structure, IBM has been quite powerful with regard to computational efficiency.

An interesting study reported by Ulrike (2003) clearly demonstrated that an analogy exists between passive flapping flag and active swimming fish. The similarity in the dynamics of both cases may not be superficial but both share a common physical mechanism governing their motion. To minimize the energy cost due to locomotion, the flag and fish modify their swimming pattern to generate motion in their natural oscillation frequency. These oscillations generate vortices in fluid around the object. The entire study clearly proves the effectiveness of studying the dynamics of passive objects to get a concise picture of their active behavior. By inducing fluid motion and analyzing the behavior of passive structures, a similar co-relation can be achieved for understanding motion and flow behavior of stationary fluid placed in an active structural deformation. Also, in studying the dynamics of flexible filaments in oscillating flow, an analogy can be developed to understand similar behavior in engineering applications such as fluid micro-mixing and micro-pumping. Zhang and Gay (2007) had studied the effect of deformation in heart-valve leaflets modeled as flexible filament at low Reynolds number for oscillating fluid flow with phase shift condition. Also, from the studies of Khatavkar *et al.* (2007) we know that phase lag in filament deformation has a tremendous influence on the surrounding fluid domain. Phase lag in a passive filament can be achieved by inducing a phase shift in the oscillatory fluid motion and its comparison with fluid motion without phase shift is another interesting study, which has not been reported earlier. Finally, by comparing studies of Khatavkar *et al.* (2007) and Lambert and Rangel (2010), we observe that channel geometry ratio and aspect ratio critically effect fluid mixing. The behavior and deformation of flexible filament and its consequence on fluid mixing for an intermediate channel geometry ratio ranging between 0.1667 and 0.48 are worth investigating. These aspects from literature serve as the prime motivation for the present study.

In this study, a two-dimensional numerical model based on a formally second-order immersed boundary framework is used to capture the fluid-structure interaction of flexible filament subjected to oscillating flow. A detailed parametric study is carried out by varying filament bending rigidity, length, Reynolds number and oscillating fluid flow conditions. The numerical method developed for this study is provided in Section 2. The numerical model is validated and simulation results of filament deformation study are provided in Section 3. Finally, conclusions are deduced in Section 4.

2. Mathematical formulation and numerical scheme

The physical problem consists of a massless and neutrally buoyant flexible filament tethered at the center of two-dimensional channel in a vertical position. The immersed boundary framework is made up of two distinct grid systems. One is a Cartesian co-ordinate system $\mathbf{x^*} = (x^*, y^*)$ that encompasses the fluid domain and other is a Lagrangian system for flexible filament structure (immersed boundary). The immersed boundary equations are written in the Lagrangian form made up of one-dimensional unknown variable $\mathbf{X}^*(s^*, t^*)$. The parameter s^* is used to assign a material point and $\mathbf{X}^*(s^*, t^*)$ describes the motion of immersed boundary along with its spatial configuration at any given time t^*. The flow variables are velocity $\mathbf{u^*}(\mathbf{x^*}, t^*)$, pressure $p^*(\mathbf{x^*}, t^*)$ and Eulerian force density $\mathbf{f^*}(\mathbf{x^*}, t^*)$ while Lagrangian force density $\mathbf{F^*}(s^*, t^*)$ is the filament variable. Two types of oscillating flow fields are used in the present study, which will be explained in detail in the next section. The equation of motion for fluid flow are given below:

$$\nabla^* . \mathbf{u}^* = 0 \tag{1}$$

$$\rho \frac{\partial \mathbf{u}^*}{\partial t^*} + \mathbf{u}^* \cdot \nabla^* \mathbf{u}^* = -\nabla^* p^* + \mu \nabla^{*2} \mathbf{u}^* + \mathbf{f}^*(\mathbf{x}^*, t^*) \tag{2}$$

where the constant μ is the fluid viscosity and ρ the fluid density.

The governing continuity and incompressible Navier–Stokes equations containing an additional force term per unit volume $\mathbf{f^*}(\mathbf{x^*}, t^*)$ are given by equations (1) and (2), respectively. These equations can be non-dimensionalized with respect to characteristic scales: filament length L_{ref}, constant inlet fluid velocity u_{ref}, scale of time t_{ref} as $\frac{L_{ref}}{u_{ref}}$, reference pressure p_{ref} as ρu_{ref}^2 and momentum forcing f_{ref} as: $\frac{\rho u_{ref}^2}{L_{ref}}$.

The resulting dimensionless equations are given as:

$$\nabla . \mathbf{u} = 0 \tag{3}$$

$$\frac{\partial \mathbf{u}}{\partial t} + \mathbf{u} \cdot \nabla \mathbf{u} = -\nabla p + \frac{1}{Re} \nabla^2 \mathbf{u} + \mathbf{f}(\mathbf{x}, t) \tag{4}$$

where,

$$Re = \frac{\rho u_{ref} L_{ref}}{\mu}$$

The extra force term $\mathbf{f}(\mathbf{x}, t)$ in equation (4), also called the momentum forcing term is the force applied to incorporate the presence of structure in the fluid domain. This forcing term is given by equation (5):

$$\mathbf{f}(\mathbf{x}, t) = \int \mathbf{F}(s, t)\ \delta\Big(\mathbf{x} - \mathbf{X}(s, t)\Big) ds \tag{5}$$

The flexible filament is made up of a number of Lagrangian points connected together by means of resistance links having resting length Δs. The function $\mathbf{F}(s, t)$ in equation (5) is the force density term, which defines the elastic or mechanical contribution of the immersed boundary on the fluid. This is given by equation (6):

$$\mathbf{F}(s,t) = -\frac{\partial E[\mathbf{X}(s,t)]}{\partial \mathbf{X}} \tag{6}$$

where the term $-\partial E/\partial \mathbf{X}$ is the variational derivative containing the elastic energy functional $E[\mathbf{X}(s, t)]$. The energy functional for the present study given in equation (7) consists of two properties. One that resists elongation/compression and another that resists bending (Zhu and Peskin, 2002). An illustration of the resultant stretching and bending forces acting on the linkages are provided in Figures 1(a) and 1(b), respectively. In the figure, X_s is the Lagrangian point surrounded by nearby points X_{s+1} and X_{s-1}:

$$E[\mathbf{X}(s,t)] = \frac{1}{2}T_{elas}\int\left(\left|\frac{\partial \mathbf{X}}{\partial s}\right| - 1\right)^2 ds + \frac{1}{2}S_{ben}\int\left|\frac{\partial^2 \mathbf{X}}{\partial s^2}\right|^2 ds \tag{7}$$

where T_{elas} and S_{ben} are the stretching co-efficient and bending co-efficient of the elastic boundary, respectively. By solving the energy functional $E[\mathbf{X}(s, t)]$, the Lagrangian force density $\mathbf{F}$ (s, t) can be calculated. Finally, the momentum forcing term in equation (5) is substituted in the governing Navier–Stokes equation (4) to produce new fluid flow variables at the next time step. Based on the newly calculated flow variables, corresponding deformation and new position of the elastic immersed boundary is obtained by substituting it in the equation of motion given by equation (8):

$$\frac{\partial \mathbf{X}}{\partial t}(s,t) = \int \mathbf{u}(\mathbf{x}, t)\ \delta(\mathbf{x} - \mathbf{X}(s,t))dx \tag{8}$$

The numerical scheme used in the present study is temporally second-order in nature. The advantage of using formally second-order scheme is that it produces results with improved accuracy (Lai and Peskin, 2000; Kim and Peskin, 2007). The total time step is divided into two stages. One is the preliminary stage and other is the final stage. In the preliminary stage, the governing equations are solved for time level $(n + \frac{1}{2})$ from data available at time level n using a first-order accurate scheme. The results of the preliminary stage are used to proceed in the final stage n to reach time level $(n + 1)$ in a formally second-order manner. If

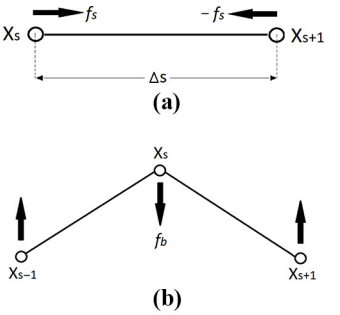

Figure 1.
The two types of filament linkages used in the present study

Notes: (a) Stretching/compression resistance linkage; (b) Bending resistance linkage between Lagrangian points

Δt is the time step, the fluid velocity for present time n is depicted as $\mathbf{u}^n$ while boundary configuration is $\mathbf{X}^n$ The objective of the numerical procedure is to compute updated $\mathbf{u}^{n+1}$ and $\mathbf{X}^{n+1}$ using the data given at time level n. As discussed above a typical time step in our formulation will proceed in two stages. In the preliminary stage from time level n to level $(\mathrm{n}+\frac{1}{2})$, the force density term $\mathbf{F}^n$ is calculated at IB points using equation (9). Further momentum forcing term $\mathbf{f}^n$ is determined at Cartesian grid points using equation (10), so as to be applied in the governing Navier–Stokes equations. This will update the fluid velocity to new time level $(\mathrm{n}+\frac{1}{2})$. The discretized form of $\mathbf{F}^n$ and $\mathbf{f}^n$ are given below as:

$$\mathbf{F}^{\mathrm{n}} = -\frac{\partial \mathrm{E}\left[\mathbf{X}^n(\mathrm{s},\mathrm{t})\right]}{\partial \mathbf{X}} \tag{9}$$

$$\mathbf{f}^{\mathrm{n}} = \sum_{\mathbf{s}} \mathbf{F}^{\mathrm{n}}(s)\ \delta_{\mathrm{h}}\left(\mathrm{x}-\mathbf{X}^{\mathrm{n}}(\mathrm{s},\mathrm{t})\right)\Delta s \tag{10}$$

where h is the Cartesian mesh width and δ_{h} is the two-dimensional Dirac delta function. In our methodology δ_{h} is chosen such that:

$$\delta_{\mathrm{h}}(\mathbf{x}) = \frac{1}{\mathrm{h}^2}\ \varphi\left(\frac{\mathrm{x}}{\mathrm{h}}\right)\ \varphi\left(\frac{\mathrm{y}}{\mathrm{h}}\right) \tag{11}$$

where φ is given by:

$$\varphi(\mathrm{r}) = \begin{cases} \frac{1}{4}\left(1+\cos\left(\frac{\pi \mathrm{r}}{2}\right)\right), & \text{if } \left|\mathrm{r}\right| \le 2, \\ 0, & \text{otherwise} \end{cases} \tag{12}$$

The Dirac delta function [equation (12)] chosen in the present work is based upon the numerical study of Maniyeri *et al.* (2012). The continuity and Navier–Stokes equations are solved next by using equations (13) and (14) given below:

$$[\nabla \cdot \mathbf{u}]^{(\mathbf{n}+1)/2} = 0 \tag{13}$$

$$\frac{\mathbf{u}^{(\mathrm{n}+1)/2}-\mathbf{u}^{\mathrm{n}}}{\left(\frac{\Delta \mathrm{t}}{2}\right)} = -\nabla \mathrm{p}^{\mathrm{n}} - [\mathbf{u}\cdot\nabla\mathbf{u}]^{\mathrm{n}} + \frac{1}{\mathrm{Re}}\nabla^2\mathbf{u}^{\mathrm{n}} + \mathbf{f}^{\mathrm{n}} \tag{14}$$

Finally, the boundary configuration is updated to new position $\mathbf{X}^{(\mathrm{n}+1)/2}$ by discretizing equation (8) as:

$$\frac{\mathbf{X}^{(\mathrm{n}+1)/2}-\mathbf{X}^{\mathrm{n}}}{\left(\frac{\Delta \mathrm{t}}{2}\right)} = \sum_{\mathbf{x}} \mathbf{u}^{(\mathrm{n}+1)/2}(\mathrm{x})\ \delta_{\mathrm{h}}\left(\mathrm{x}-\mathbf{X}^{\mathrm{n}}(\mathrm{s},\mathrm{t})\right)\mathrm{h}^2 \tag{15}$$

This concludes the preliminary stage. The final stage starts again at time level n to reach level $\mathrm{n}+1$ using intermediate variables $\mathbf{u}^{(\mathrm{n}+1)/2}$ and $\mathbf{X}^{(\mathrm{n}+1)/2}$ obtained from the preliminary

stage. First, the Lagrangian force density $\mathbf{F}^{(n+1)/2}$, which consists of elastic forces acting on immersed boundary points is discretized and calculated as:

$$\mathbf{F}^{(n+1)/2} = -\frac{\partial E\left[\mathbf{X}^{(n+1)/2}\right]}{\partial \mathbf{X}} \tag{16}$$

Next, the Eulerian force density is calculated, which is obtained by discretizing equation (5) as:

$$\mathbf{f}^{(n+1)/2} = \sum_{\mathbf{s}} \mathbf{F}^{(n+1)/2}(s)\ \delta_h\left(x - \mathbf{X}^{(n+1)/2}(s,t)\right)\Delta s \tag{17}$$

Finally, the fluid velocity $\mathbf{u}^{(n+1)/2}$ is updated to new time $(n+1)$ and shown below:

$$[\nabla . \mathbf{u}]^{\mathbf{n}+1} = 0 \tag{18}$$

$$\frac{\mathbf{u}^{n+1} - \mathbf{u}^{n}}{\Delta t} = -\nabla p^{(n+1)/2} - [\mathbf{u}\cdot\nabla\mathbf{u}]^{(n+1)/2} + \frac{1}{Re}\nabla^2\mathbf{u}^{(n+1)/2} + \mathbf{f}^{(n+1)/2} \tag{19}$$

Using this new fluid velocity value, the boundary configuration $\mathbf{X}^{n+1}$ is updated as:

$$\frac{\mathbf{X}^{n+1} - \mathbf{X}^{n}}{\Delta t} = \sum_{\mathbf{x}} \mathbf{u}^{n+1}(x)\ \delta_h\left(x - \mathbf{X}^{(n+1)/2}(s,t)\right)h^2 \tag{20}$$

This marks the end of the final stage. As the present IBM is temporally second-order in nature, we use two steps in the numerical procedure. For better understanding, a step by step immersed boundary implementation is provided below:

Step 1: By using the variables $\mathbf{u}^n$ and $\mathbf{X}^n$ available at present time level *n*, the force density $\mathbf{f}^n$ is calculated at IB points using equations (9) and (10) with the Dirac delta function given by equations (11) and (12).

Step 2: The force density term $\mathbf{f}^n$ calculated in Step 1 is added to the Navier–Stokes equation and fluid velocity $\mathbf{u}^{(n+1)/2}$ is determined by solving equations (13) and (14).

Step 3: The new boundary configuration $\mathbf{X}^{(n+1)/2}$ is calculated next using equation (15). This marks the end of preliminary stage.

Step 4: The variables $\mathbf{u}^{(n+1)/2}$ and $\mathbf{X}^{(n+1)/2}$ available at preliminary stage [time level $(n+1)/2$] are used to determine force density term $\mathbf{f}^{n+1}$, fluid velocity $\mathbf{u}^{n+1}$ and filament displacement $\mathbf{X}^{n+1}$ using equations (16)-(20). This marks the end of final stage [time level $(n+1)$].

Step 5: The Steps 1-4 are repeated and the filament positions are evolved with time."

The Cartesian grid covering the fluid domain is arranged in a staggered manner. The time advancement approach is implicit and the discretization is based on finite volume method (FVM). The convection and diffusion fluxes obtained from FVM discretization of governing equations are treated using a second-order differencing technique called method of deferred correction. This technique was described by Hayase *et al.* (1992) to maintain linearity and diagonal dominance of iterative solver and also to prevent oscillation of numerical solutions. The source term is modified to contain difference between first-order upwind scheme and second-order central differencing. A second-order central difference scheme is used to

discretize the spatial derivatives. SIMPLE algorithm is used to solve the continuity and momentum equations. Initially, the fluid pressure is guessed and an intermediate velocity is calculated. A pressure Poisson equation is used to correct pressure and maintain continuity. The Incomplete Cholesky Conjugate Gradient (ICCG) method is used to solve the pressure equation. The input to the Poisson pressure correction equation is the intermediate velocity calculated previously. The corrected pressure and initial guessed pressure values are added together to obtain the actual pressure in the system. Using this, the actual flow velocity variable in x and y directions are obtained and the solution is kept divergence free. No-slip boundary conditions are applied to the top and bottom channel walls. Periodic boundary condition is applied at the inlet and outlet of channel and flow is driven by an oscillating pressure gradient, details of which will be provided in subsequent sections.

3. Results and discussion

3.1 Validation

The numerical model discussed in the previous section has already been validated and verified in the previous study involving flexible filament in uniform and shear flow conditions (Kanchan and Maniyeri, 2019). We further validate the model with numerical works of Zhang and Gay (2007), who studied the behavior of flexible leaflet subjected to sinusoidally oscillatory fluid flow with phase shift using immersed finite element method. Accordingly, in the present study, the leaflet is modeled as a one-dimensional filament, which is made up of connected spring systems, each having fixed stretching and bending stiffness. The two-dimensional rectangular fluid domain has a height of 1.0 and length 4.0. The leaflet is placed vertically and leading-edge is fixed to the center of the channel at a location $X_0 = (2, 0)$ while trailing edge is free to move in fluid flow direction. The length of the leaflet is fixed as 0.8. The initial position of the filament is maintained at $\theta = 90°$. A schematic representation of flexible filament tethered at the center of channel in oscillating flow condition along with boundary conditions are provided in Figure 2. The length of the channel is taken as L_c and height as H.

Before considering the solution to the validation problem, the inextensibility of the leaflet modeled as a flexible filament has to be ascertained. The inextensibility condition governs the extension of the filament, thus, preventing it from undergoing spurious stretching or deformations. Failure to maintain the condition causes oscillating instability in the solution scheme. As the tension and bending forces are calculated explicitly in the formulation, a large value of T_{elas} is considered while S_{ben} remains constant at 1.0. Numerical stability of the method can be maintained for large values of T_{elas} provided there is a small time step.

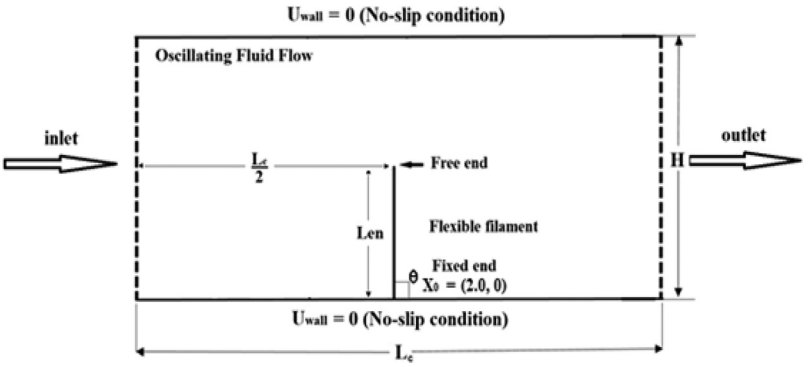

Figure 2.
Schematic diagram of flexible tethered filament placed in viscous oscillating fluid flow

Hence, the time step Δt for the present study is fixed as 1×10^{-5}. A length error $\varepsilon(t)$, is calculated, which determines the deviation of filament length from original value. It is given by equation (21):

$$\varepsilon\,(\mathrm{t}) = \max\left|\frac{\partial \mathbf{X}}{\partial \mathrm{s}} . \frac{\partial \mathbf{X}}{\partial \mathrm{s}} - 1\right| \tag{21}$$

Comparison of average length error (ε) indicating elongation and compression behavior of flexible filament for different stretching co-efficient (T_{elas}) values over total simulation time, t = 3.0 is provided in Table I. There is deviation of 3.67 per cent between T_{elas} = 1,000 and T_{elas} = 10,000 length error values. Thus, an optimum value of T_{elas} = 10,000 is fixed, which maintains the inextensibility condition. The inextensible error equation is taken from a simulation study of flexible filament in uniform flow by Huang *et al.* (2007). Their methodology strictly enforces the filament inextensibility condition implicitly with no restrictions on time step. Next, the refinement of the computational grid is carried out by performing a grid convergence test. Based on inextensibility test data, three cases of uniform Eulerian grids in x and y direction are considered and their average length error over a simulation time t = 3.0 is recorded in Table II. The percentage change in length error between the first and second grid size is found to be 19 per cent while that between the second and third is 2.1 per cent. As the later difference in average error is marginal as compared to the first and second grid difference and to minimize computational time, the best possible configuration of the fluid grid for the present study is chosen to be 512 × 128. With reference to grid convergence study and inextensibility tests, two-dimensional numerical simulation of flexible leaflet subjected to pressure-driven oscillating flow is carried out, similar to leaflet deformation of Zhang and Gay (2007). The filament is massless and its physical thickness is not considered in our study. The Reynolds number is fixed at 10.0 and the total simulation time is 3.0. The motion of filament is examined for two different Strouhal numbers (St) of 0.5 and 1.0, respectively, where St is given by equation (22):

Table I.
Comparison of average length error (ε) for varying time step (Δt) and varying stretching co-efficient (t_{elas}) for fixed value of bending co-efficient (s_{ben} = 1.0)

Stretching co-efficient (T_{elas})	Time step (Δt)	Average length error (ε)
1,000	1.0×10^{-4}	9.33×10^{-4}
2,500	1.0×10^{-5}	9.30×10^{-4}
5,000	1.0×10^{-5}	9.20×10^{-4}
7,500	1.0×10^{-5}	9.08×10^{-4}
10,000	1.0×10^{-5}	9.0×10^{-4}

Table II.
Comparison of average length error (ε) with different uniform Eulerian grids in x and y direction

Grids	Time step (Δt)	Average length error (ε)
256 × 64	1.0×10^{-5}	1.07×10^{-3}
512 × 128	1.0×10^{-5}	9.0×10^{-4}
1,024 × 256	1.0×10^{-5}	8.81×10^{-4}

$$\mathrm{St} = \frac{\mathrm{f\,H}}{\mathrm{U_{ref}}} \tag{22}$$

where, f = frequency of oscillation. The fluid is driven by a sinusoidal pressure gradient in positive x-direction defined by equation (23):

$$\frac{\Delta p}{L} = \frac{12}{\mathrm{Re}} \times \sin(\ \pi \mathrm{ft} + \ \pi/2) \tag{23}$$

The tip velocity of the filament at St = 0.5 and St = 1.0 are shown in Figures 3 and 4, respectively, and compared with the works of Zhang and Gay (2007). The results are also found to be in close agreement, which depicts the validity of the developed model.

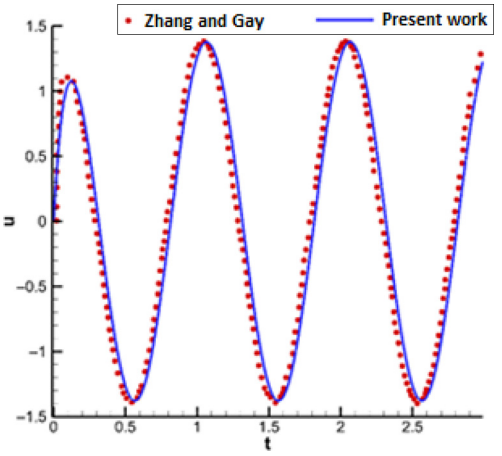

Figure 3.
Filament tip velocity comparison of present study with work of Zhang and Gay (2007) at Re = 10.0 and St = 1.0

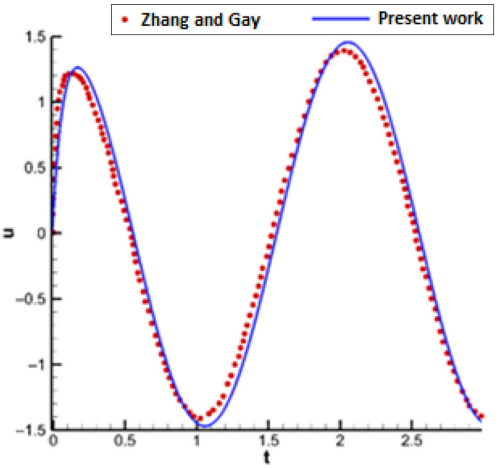

Figure 4.
Filament tip velocity comparison of present study with work of Zhang and Gay (2007) at Re = 10.0 and St = 0.5

3.2 Filament deformation parametric study

The behavior of the vertically fixed flexible filament shown in Figure 2, subjected to pressure-driven oscillating fluid flow is studied. A parametric analysis is carried out for three filament lengths, Len = 0.4, 0.6 and 0.8, two bending rigidities, $S_{ben} = 1 \times 10^{-3}$ and 1×10^{-4} and three different Reynolds numbers, Re = 50, 75 and 100. Two types of oscillating fluid flow conditions are considered for fixed filament length, Len = 0.8 and St = 0.5. The first type is sinusoidally oscillatory flow with phase shift (SOFPS as discussed in the validation study given by equation (23). The second is sinusoidally oscillatory flow without phase shift (SOF), which is given by equation (24):

$$\frac{\Delta p}{L} = \frac{12}{\mathrm{Re}} \times \sin(\ \pi \mathrm{ft}) \tag{24}$$

A series of velocity vector plots depicting the motion of fluid for a total time period t = 1.0 is provided in Figures 5 and 6 for SOFPS and SOF flow conditions, respectively. For SOFPS fluid flow conditions, zero fluid velocities are observed at t = 0.0, 0.3 and 0.8, whereas zero fluid velocities are observed at t = 0.0, 0.5 and 1.0 for SOF condition. The fluid reaches maximum velocity value of 1.38, two times in the positive cycle for SOFPS flow condition while minimum fluid velocity of −1.38 is achieved only once in the negative cycle spanning the entire time period. However, an observation of velocity vectors corresponding to SOF condition shows that fluid attains positive and negative cycle only once during the time

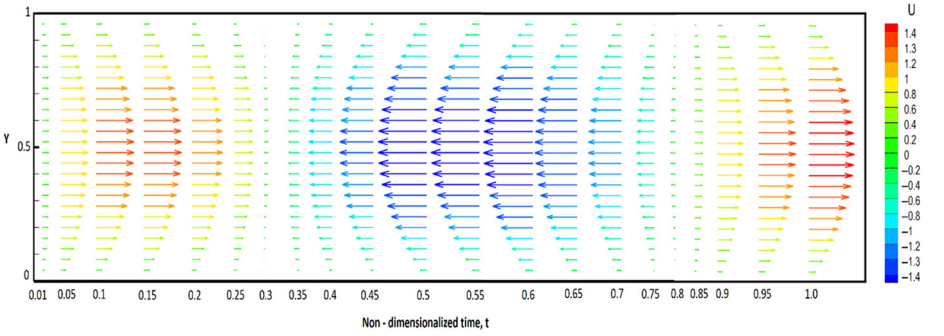

Figure 5.
Series of velocity vector plots obtained at channel location x = 2.0 for different non-dimensionalized time sequences taking SOFPS flow condition

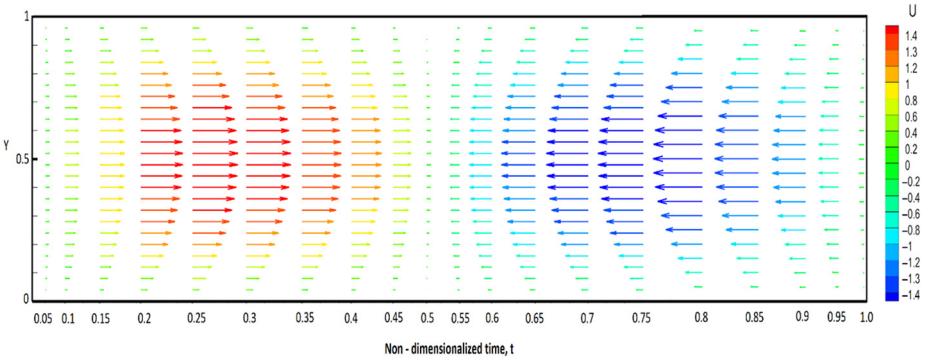

Figure 6.
Series of velocity vector plots obtained at channel location x = 2.0 for different non-dimensionalized time sequences taking SOF flow condition

period. The magnitude of maximum and minimum velocities remains the same for both flow conditions. Hence, both these flow condition will have varying effects on filament displacement and dynamics. The flexible filament is placed vertically and tethered at the center of the rectangular channel of height, H = 2.0 and length, L_c = 8.0, which produces a channel geometry ratio (H/L_c) = 0.25. The effect of varying filament length, bending rigidity, Reynolds number and flow conditions are ascertained with the help of the parametric study. A detailed discussion is provided below.

The presence of flexible filament in the fluid region is analyzed by plotting the X-component and Y-component of velocity. Figures 7-9 shows the X-component of velocity for different filament lengths at time t = 3.48, 3.72 and 3.96, respectively. The results are

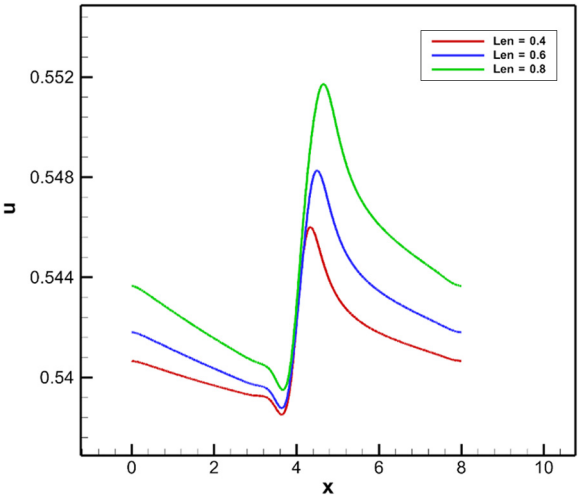

Figure 7.
X-component of velocity at time, t = 3.48 plotted with respect to channel length along the channel y-centerline for different filament length, Len = 0.4, 0.6, 0.8 at Reynolds number, Re = 100 and fixed bending rigidity, $S_{ben} = 1 \times 10^{-4}$

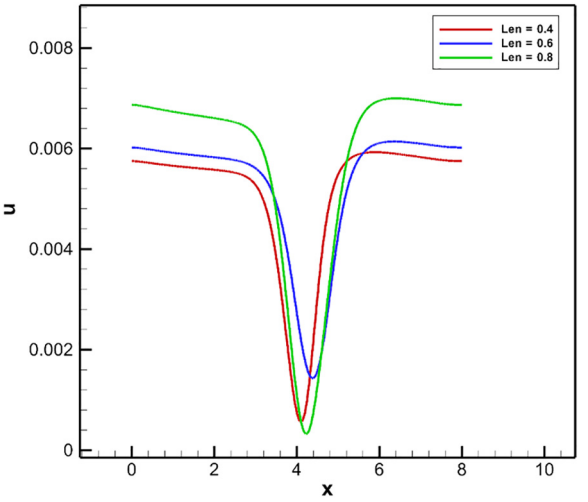

Figure 8.
X-component of velocity at time, t = 3.72 plotted with respect to channel length along the channel y-centerline for different filament length, Len = 0.4, 0.6, 0.8 at Reynolds number, Re = 100 and fixed bending rigidity, $S_{ben} = 1 \times 10^{-4}$

plotted with respect to channel length along the y-centerline of channel for Re = 100. As shown in Figures 7-9, sharp deviation in velocity is observed at channel mid-length position, due to presence of filament. The magnitude of the deviation increases for an increase in filament length. Similar deviation in velocity is also observed in Y-component of velocity shown in Figures 10-12 caused by the presence of flexible filament. However, there is no significant difference in deviations between filament lengths as compared to X-component velocities. This also indicates that the effect of increasing filament length has more impact in the longitudinal direction as compared to the transverse direction. Next, the effect on fluid velocity by varying bending rigidity of the filament is determined by plotting X and Y-components of velocity as shown in Figures 13-14, respectively. In both the figures, we see

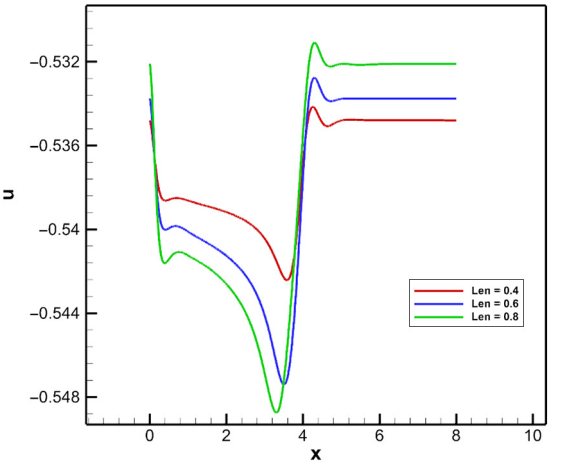

Figure 9.
X-component of velocity at time, t = 3.96 plotted with respect to channel length along the channel y-centerline for different filament length, Len = 0.4, 0.6, 0.8 at Reynolds number, Re = 100 and fixed bending rigidity, $S_{ben} = 1 \times 10^{-4}$

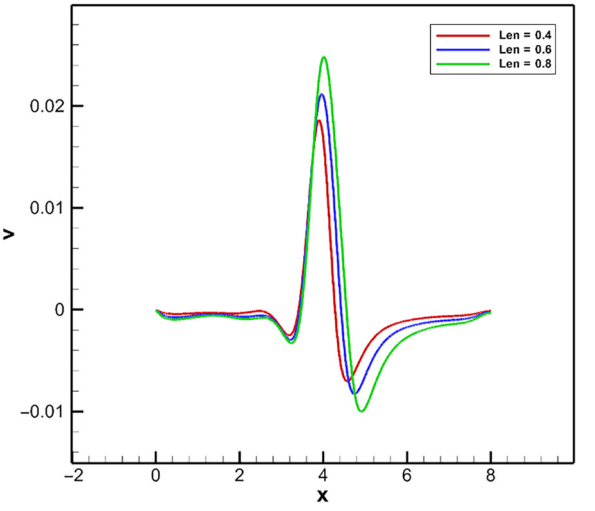

Figure 10.
Y-component of velocity at time, t = 3.48 plotted with respect to channel length along the channel y-centerline for different filament length, Len = 0.4, 0.6, 0.8 at Reynolds number, Re = 100 and fixed bending rigidity, $S_{ben} = 1 \times 10^{-4}$

that there is an appreciable difference in a deviation between filaments with different rigidities. Rigid filaments tend to have a much higher influence in the longitudinal and transverse direction as compared to flexible filaments. The filament dynamics is, thus, strongly governed by filament length and bending rigidity.

Another way of understanding the filament dynamics and its corresponding effect on the fluid domain is by observing the instantaneous filament deformations and streamlines for different filament lengths and bending rigidity. The hydrodynamic forces have a great influence on filament bending or deformation. Figures 15 and 16 shows the filament deformation for filament length, Len = 0.4 in the positive x-direction for different rigidities at Re = 100. Flexible filament produces a full symmetrical sweeping pattern with good

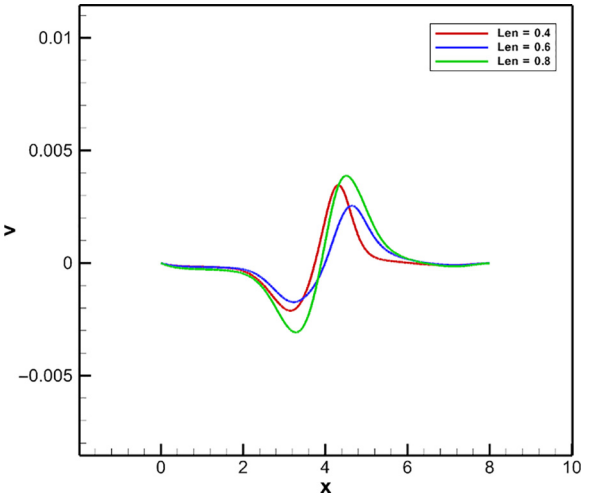

Figure 11.
Y-component of velocity at time, t = 3.72 plotted with respect to channel length along the channel y-centerline for different filament length, Len = 0.4, 0.6, 0.8 at Reynolds number, Re = 100 and fixed bending rigidity, $S_{ben} = 1 \times 10^{-4}$

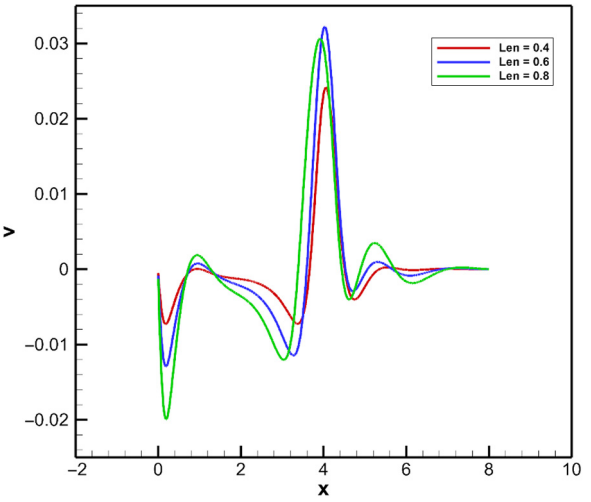

Figure 12.
Y-component of velocity at time, t = 3.96 plotted with respect to channel length along the channel y-centerline for different filament length, Len = 0.4, 0.6, 0.8 at Reynolds number, Re = 100 and fixed bending rigidity, $S_{ben} = 1 \times 10^{-4}$

extensions in the x-direction, whereas the rigid filament has a retarded extension and has a smaller sweep span. This retardation is due to the dominance of elastic forces over hydrodynamic forces. The filament exhibits higher resistance to fluid motion. The implications of these two types of filament deformation on the fluid region are observed by looking at the streamline plots in Figures 17 and 18. Observing Figure 17, a recirculation zone is created behind the filament in its immediate vicinity and the filament obstructs zone formations in the opposite direction. On the other hand, in Figure 18, the recirculation zone extends out along the length of the channel, behind and in front of the filament due to the

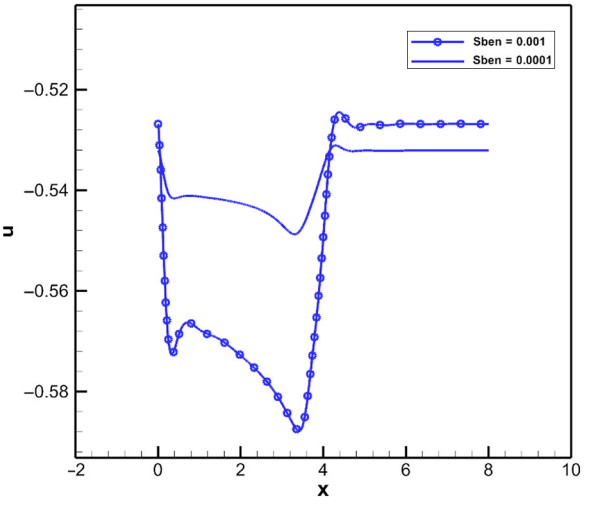

Figure 13.
X-component of velocity at time, t = 3.96 plotted with respect to channel length along the channel y-centerline for different bending rigidities, $S_{ben} = 1 \times 10^{-3}, 1 \times 10^{-4}$ at Reynolds number, Re = 100 and fixed filament length, Len = 0.8

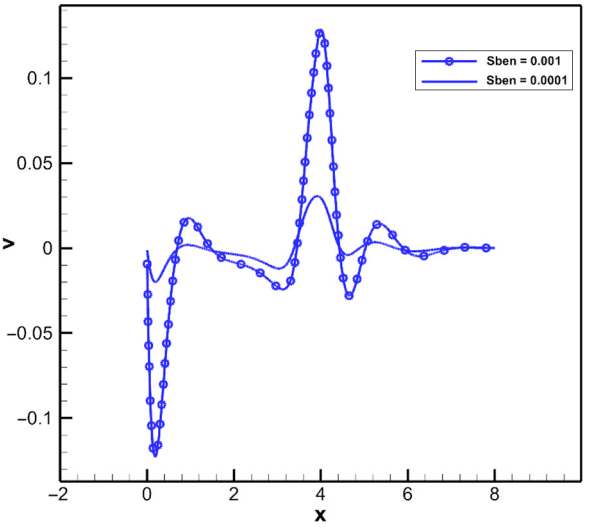

Figure 14.
Y-component of velocity at time, t = 3.96 plotted with respect to channel length along thechannel y-centerline for different bending rigidities, $S_{ben} = 1 \times 10^{-3}, 1 \times 10^{-4}$ at Reynolds number, Re = 100 and fixed filament length, Len = 0.8

symmetrical sweeping pattern. The size of the recirculation zone, however, is restricted to the lower half portion of the channel and no considerable mixing is observed above the filament.

Figures 19 and 20 shows the filament deformation for filament length, Len = 0.6 in the positive x-direction for different rigidities at Re = 100. Retarded motion for rigid filament and sweeping motion for flexible filament is seen here as well. The symmetrical sweeping pattern in the flexible filament is accompanied by bending deformation. A similar phenomenon in streamlines as observed in Figure 17 is also found in Figure 21. Looking at the streamlines obtained in Figure 22, the recirculation zones extend out in the longitudinal

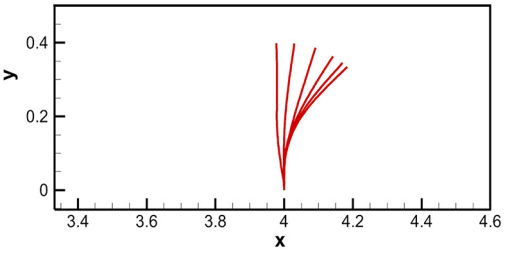

Figure 15.
Instantaneous filament deformations in positive x-direction for fixed filament length, Len = 0.4 and fixed bending rigidity, $S_{ben} = 1 \times 10^{-3}$ at Reynolds number, Re = 100

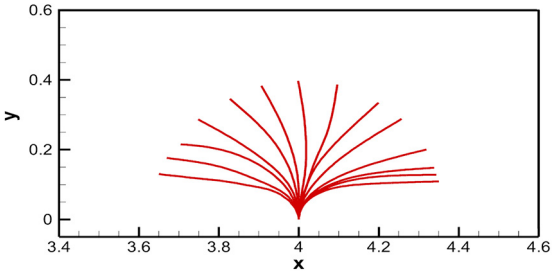

Figure 16.
Instantaneous filament deformations in positive x-direction for fixed filament length, Len = 0.4 and fixed bending rigidity, $S_{ben} = 1 \times 10^{-4}$ at Reynolds number, Re = 100

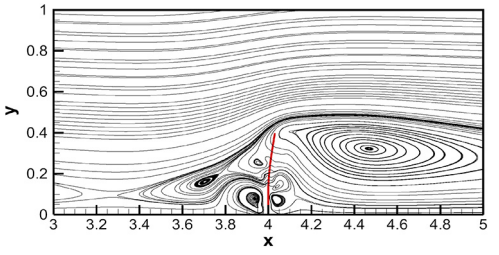

Figure 17.
Streamlines obtained at the vicinity of filament for fixed filament length, Len = 0.4 and fixed bending rigidity, $S_{ben} = 1 \text{ X } 10^{-3}$ at Reynolds number, Re = 100

direction. Also, the size of the zone is larger covering a major portion of channel. Even though the top area of the channel does not see any recirculation zone formations, the mixing is much better for this case as compared to the smaller filament. Finally, the instantaneous deformations and streamline for filament length, Len = 0.8 are shown in Figures 23-26. As we can see in Figures 23 and 24, there is no form of retardation in filament motion. Symmetrical sweeping motion is seen for both rigid and flexible filament. There exists a balance between elastic and hydrodynamics forces, which produces the symmetrical sweep motion in rigid filament. Due to higher filament length, flexible filament tends to produce appreciable bending deformation. This also indicates that due to lower

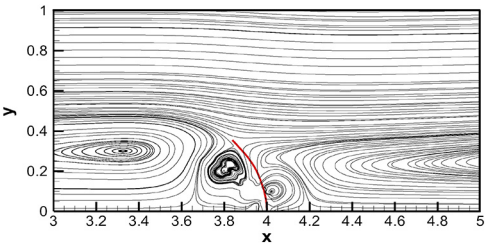

Figure 18.
Streamlines obtained at the vicinity of filament for fixed filament length, Len = 0.4 and fixed bending rigidity, $S_{ben} = 1 \times 10^{-4}$ at Reynolds number, Re = 100

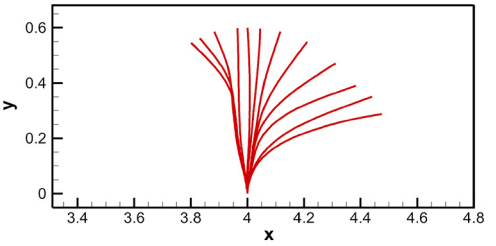

Figure 19.
Instantaneous filament deformations in positive x-direction for fixed filament length, Len = 0.6 and fixed bending rigidity, $S_{ben} = 1 \times 10^{-3}$ at Reynolds number, Re = 100

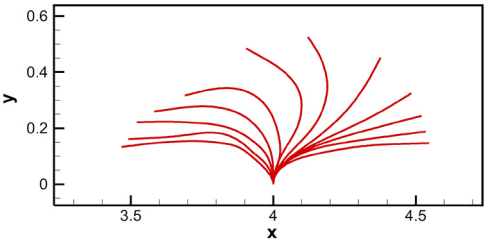

Figure 20.
Instantaneous filament deformations in positive x-direction for fixed filament length, Len = 0.6 and fixed bending rigidity, $S_{ben} = 1 \times 10^{-4}$ at Reynolds number, Re = 100

rigidity, the effect of hydrodynamic forces on the filament is stronger and the filament shows the least resistance to deformation. In Figure 25, we see that due to the sweeping filament motion the recirculation zones are formed along the channel length. Additionally, a large recirculation zone is formed in front of the filament covering the transverse extent of the channel. These recirculation zones are generally formed when there is opposition to fluid motion. This opposition to fluid motion is in turn caused by flap bending motion formed by fluid resistance. There is a better distribution of recirculation zones for a larger portion of channel geometry. However, the same is not true for flexible filament case (Figure 26). There are hardly any recirculation zones at the top and bottom channel portion indicating poor mixing capability.

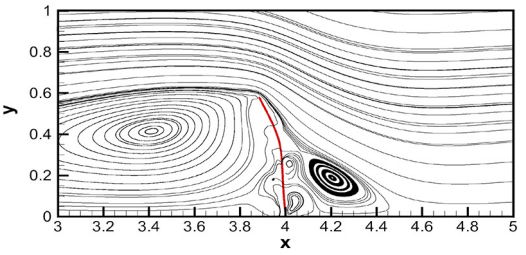

Figure 21.
Streamlines obtained at the vicinity of filament for fixed filament length, Len = 0.6 and fixed bending rigidity, $S_{ben} = 1 \times 10^{-3}$ at Reynolds number, Re = 100

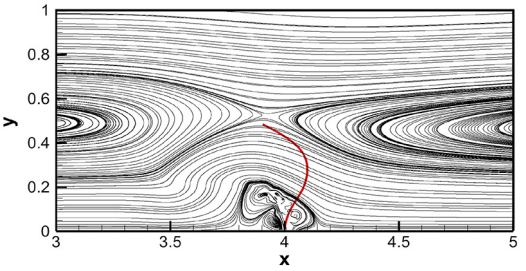

Figure 22.
Streamlines obtained at the vicinity of filament for fixed filament length, Len = 0.6 and fixed bending rigidity, $S_{ben} = 1 \times 10^{-4}$ at Reynolds number, Re = 100

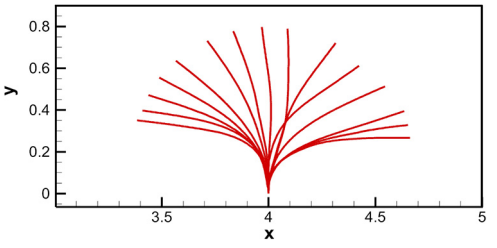

Figure 23.
Instantaneous filament deformations in positive x-direction for fixed filament length, Len = 0.8 and fixed bending rigidity, $S_{ben} = 1 \times 10^{-3}$ at Reynolds number, Re = 100

We have realized that filament sweep or flap dynamics has a tremendous impact on the surrounding fluid motion. The flap dynamics can be further quantified by measuring the angle θ made by the filament with respect to the horizontal during its sweep motion. Every parametric variation either filament length, bending rigidity or Reynolds number significantly effects sweeping time. To get a better understanding of this scenario, a probability distribution φ indicating the time spent by the flexible filament at various angles θ is calculated for all parametric test cases. It also provides a measure of the sweep span related to filament deformation for all cases. Figure 27 depicts the probability distribution with respect to angle θ for three different filament lengths and two bending rigidities at Re = 50. The probability peaks also show the least angle attained by the filament during its alignment parallel to the horizontal. Such alignments are usually seen

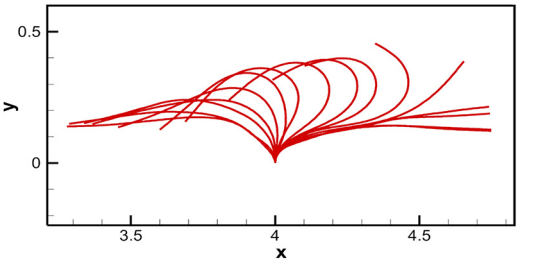

Figure 24.
Instantaneous filament deformations in positive x-direction for fixed filament length, Len = 0.8 and fixed bending rigidity, $S_{ben} = 1 \times 10^{-4}$ at Reynolds number, Re = 100

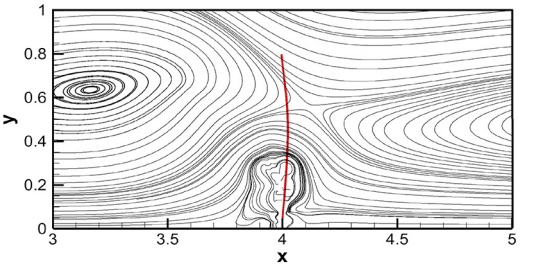

Figure 25.
Streamlines obtained at the vicinity of filament for fixed filament length, Len = 0.8 and fixed bending rigidity, $S_{ben} = 1 \times 10^{-3}$ at Reynolds number, Re = 100

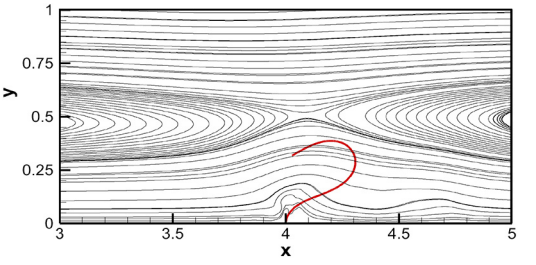

Figure 26.
Streamlines obtained at the vicinity of filament for fixed filament length, Len = 0.8 and fixed bending rigidity, $S_{ben} = 1 \times 10^{-4}$ at Reynolds number, Re = 100

during the end of positive or negative cycles. As shown in Figure 27, rigid filaments show a greater probability of retaining large-angle θ. This is seen by comparing the distribution peaks for all the cases. It also proves the retarded filament deformation observed for rigid filaments of length, Len = 0.4 and 0.6. Flexible filaments, on the other hand, produce better sweeping motion, thus, showing a finer distribution. The distribution peaks for flexible filaments are more toward lower angles θ, thus, capturing the flapping span. Flexible filaments of all lengths have a similar span, whereas the flapping span for rigid filaments keep increasing as length increases. The effect of varying fluid flow conditions on flexible filaments of different length subjected to higher Reynolds number, Re = 100 is shown in Figure 28. We see that for higher Reynolds number, the span of the filament sweep keeps increasing as filament length increases. Also, when comparing filaments of same length, Len = 0.8 subjected to SOF and SOFPS flow conditions, the filament span for both cases are similar with the exception that filament subjected to SOFPS condition remains in the lowest angle position for a larger portion of time. Similar observations are also seen in Figures 29

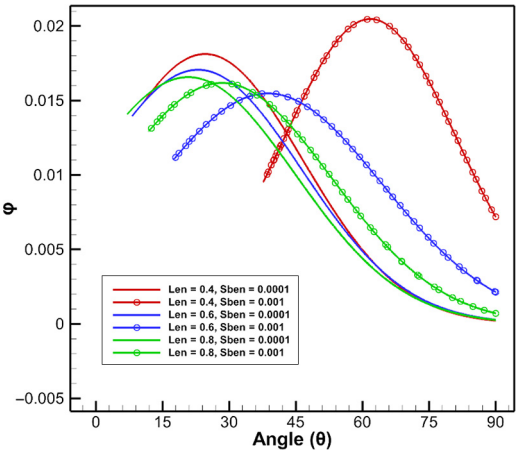

Figure 27. Probability distribution of time spent by flexible filament at various angles for filament lengths, Len = 0.4, 0.6, 0.8 and bending rigidities, $S_{ben} = 1 \times 10^{-3}, 1 \times 10^{-4}$ at Reynolds number, Re = 50

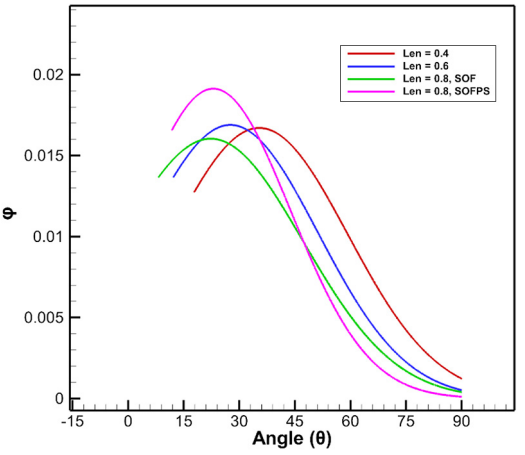

Figure 28. Probability distribution of time spent by flexible filament at various angles for filament lengths, Len = 0.4, 0.6, 0.8 and fixed bending rigidity, $S_{ben} = 1 \times 10^{-4}$ at Reynolds number, Re = 100

and 30 where the rigid and flexible filaments are compared for different Reynolds numbers at different fluid flow conditions. Also, in Figure 29, we see that the sweep span of rigid filament keeps decreasing as Reynolds number increases, whereas in flexible filament (Figure 30), the sweep span remains constant irrespective of changing Reynolds number.

The effect of Reynolds number on the sweep pattern can be further analyzed by comparing the minimum angle and mean angle produced by the filament for various filament lengths, bending rigidity and flow conditions as shown in Figures 31-36. Figures 31-33 compares different bending rigidities for individual filament lengths. Figure 12(d) Figures 34 looks at a particular case where SOFS flow condition is concerned. In Figures 35 and 36, the comparison of mean and minimum angle is carried out for fixed length, Len = 0.8 subjected to different oscillating flow conditions. By looking at all the figures, we find that the mean and minimum angles keep increasing as Reynolds number increases irrespective of filament length. Rigid filaments have higher mean and minimum angles as compared to flexible filaments for all cases. It is possible to categorize filament deformation patterns by

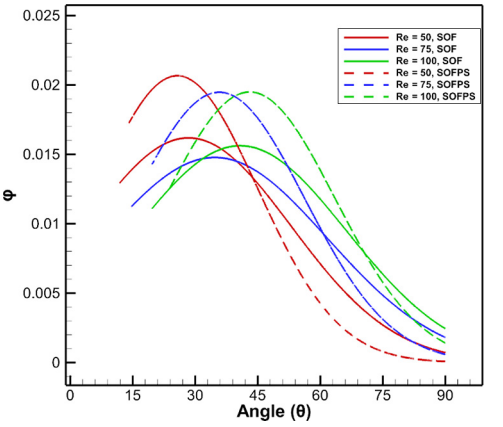

Figure 29.
Comparison of SOF and SOFPS flow conditions at different Reynolds numbers, Re = 50, 75, 100 using probability distribution plot of time spent by the flexible filament at various angles for fixed filament length, Len = 0.8 and fixed bending rigidity, $S_{ben} = 1 \times 10^{-3}$

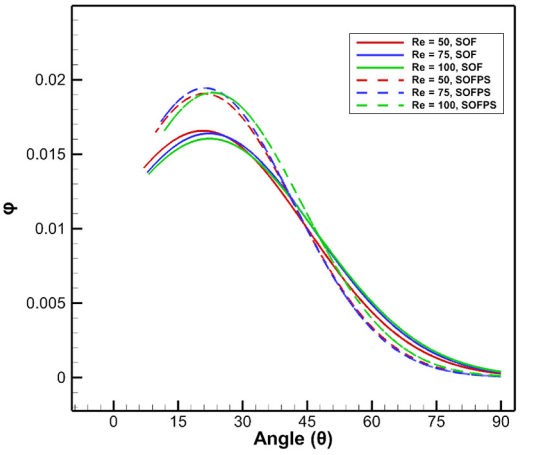

Figure 30.
Comparison of SOF and SOFPS flow conditions at different Reynolds numbers, Re = 50, 75,100 using probability distribution plot of time spent by the flexible filament at various angles for fixed filament length, Len = 0.8 and fixed bending rigidity, $S_{ben} = 1 \times 10^{-4}$

calculating the slope of mean angle curve. The slope of mean angle curve generated by the flapping of flexible filaments is calculated for all filament lengths from Figures 31-36. The values are tabulated in Table III along with their corresponding lengths, bending rigidity and flapping patterns. From the details observed in Table III, we see that filaments producing symmetrical sweep pattern have a slope of mean angle θ curve value ranging between 0.09 and 0.35. The slope values existing outside this range produces either a retarded deformation or filament sweep with an appreciable bend. The above slope values are obtained for a fixed channel geometry ratio of 0.25, Reynolds number ranging from 50 to 100 and aspect ratios ranging from 0.2 to 0.4. Further investigation is required to determine the range of slope values for different filament lengths, bending rigidity and Reynolds number as there is a possibility of changes in slope value range according to parametric variations. From the present study we demonstrate that by calculating the slope of mean angle θ curves, filament deformation patterns can be easily categorized.

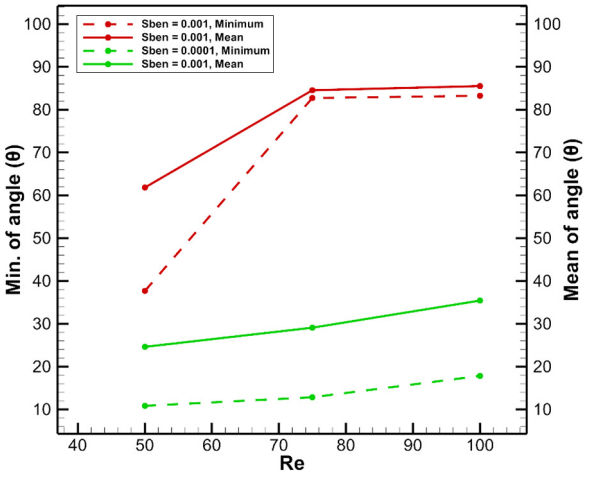

Figure 31.
The mean and minimum angle attained by the filament with respect to different Reynolds number for fixed filament length, Len = 0.4 and bending rigidities, $S_{ben} = 1 \times 10^{-3}$, 1×10^{-4}

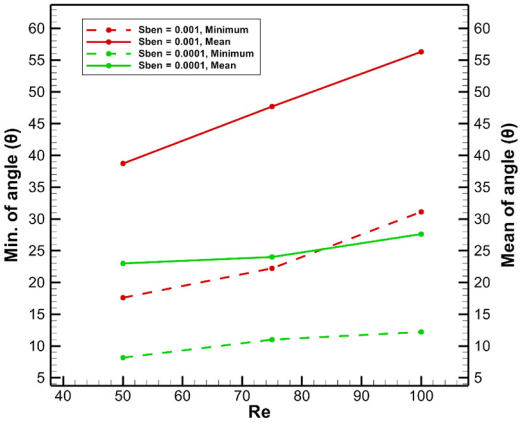

Figure 32.
The mean and minimum angle attained by the filament with respect to different Reynolds number for fixed filament length, Len = 0.6 and bending rigidities, $S_{ben} = 1 \times 10^{-3}$, 1×10^{-4}

The extent of filament flap can be characterized by looking at the trajectory of filament tip as shown in Figures 37 and 38. The figure in 37 provides the trajectory for rigid filaments of different filament lengths at Re = 100. It is evident from the figure that filaments with length, Len = 0.4 and 0.6 show retarded motion, whereas Len = 0.8 shows a full sweeping pattern. When observing flexible filaments in Figure 38, the trajectories for length, Len = 0.6 and 0.8 results in the octave-shaped pattern. Such patterns were also observed in beating cilia studies of Dauptain *et al.* (2008). The size of the pattern increases with filament length. It also provides an indication of appreciable filament bend observed for both these length cases. Figures 39 and 40 shows the filament tip displacement with fixed filament length, Len = 0.8 for varying Reynolds number considering rigid and flexible filaments, respectively. A flattened behavior in tip displacement is observed for all cases, which indicated that filament remains aligned in the fluid flow direction. The path followed by tip displacement is similar irrespective of changing Reynolds number for both rigid and flexible filaments. Figures 41 and 42 shows the effect of filament length on tip displacement for rigid

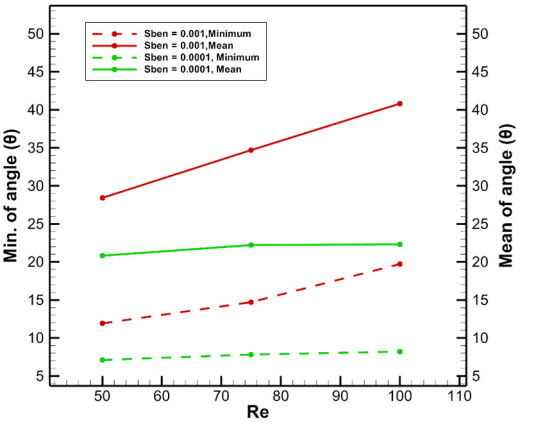

Figure 33.
The mean and minimum angle attained by the filament with respect to different Reynolds number for fixed filament length, Len = 0.8 and bending rigidities, $S_{ben} = 1 \times 10^{-3}$, 1×10^{-4}

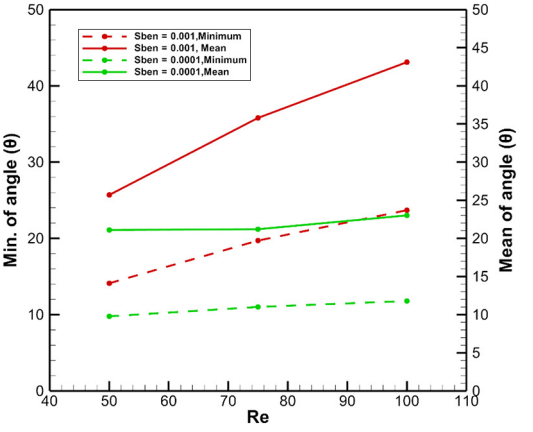

Figure 34.
The mean and minimum angle attained by the filament with respect to different Reynolds number for fixed filament length, Len = 0.8 and bending rigidities, $S_{ben} = 1 \times 10^{-3}, 1 \times 10^{-4}$ for SOFPS flow condition

and flexible filaments, respectively at Re = 50. The trajectory path is different for individual filaments as they belong to different length categories. As expected, the longest filament shows the highest displacement irrespective of rigidity. When comparing filament of length, Len = 0.4 for both rigid and flexible case, we observe that the trajectory path for rigid filament gets staggered near channel mid-length as compared to flexible filament were the profile is smooth. This may be due to the retarded deformation experienced by rigid filaments of lower filament length. Increasing the Reynolds number to 100 has a different effect on tip trajectory as shown in Figures 43 and 44. There is a clear difference in sweep dynamics for rigid filaments with different length (Figure 43). Filaments belonging to length, Len = 0.4 and 0.6 show no displacement below channel mid-plane, thus, showing a retarded pattern. Higher length filament (Len = 0.8) shows displacement both above and below mid-plane, thus, indicating sweep pattern. When comparing rigid filaments in Figures 41 and 43, we see that as Reynolds number increases, there is greater retardation of filament displacement for lower filament lengths. The filaments show higher resistance to hydrodynamic forces. Finally, we compare rigid and flexible filaments subjected to SOF and

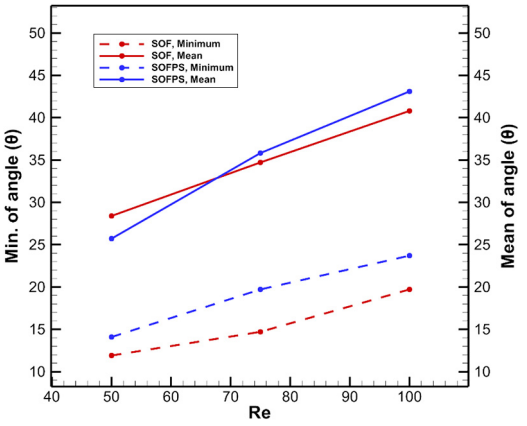

Figure 35.
SOF and SOFPS flow condition comparison of mean and minimum angle attained by the filament with respect to different Reynolds number for fixed filament length, Len = 0.8 and fixed bending rigidity, $S_{ben} = 1 \times 10^{-3}$

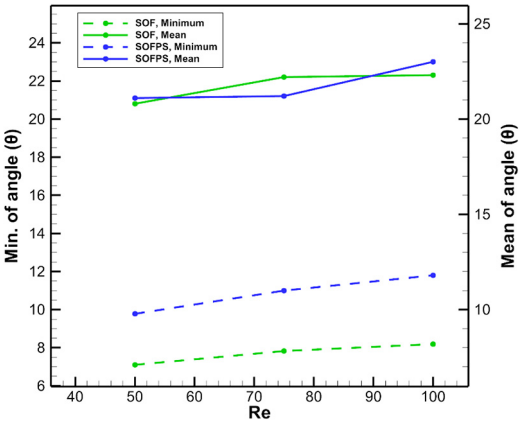

Figure 36.
SOF and SOFPS flow condition comparison of mean and minimum angle attained by the filament with respect to different Reynolds number for fixed filament length, Len = 0.8 and fixed bending rigidity, $S_{ben} = 1 \times 10^{-4}$

SOFPS flow conditions in Figure 45. Irrespective of the flow conditions, rigid filament has lower displacement as compared to flexible filament. Due to the phase shift in fluid flow, we observe a shift in x-direction tip displacement for rigid and flexible filaments. The displacement path for flexible filaments are quite similar for both the fluid conditions. However, rigid filaments subjected to SOFPS flow condition has a lower sweep span as compared to filaments in SOF condition.

Filaments of length, Len = 0.8 producing symmetrical sweep patterns help in better distribution of recirculation zones for a larger portion of channel geometry. The presence of such recirculation zones is beneficial for chaotic fluid mixing applications (Anand *et al.*, 2017). From, the above discussions on parametric studies it is clear that a minimum aspect ratio (Len/H) of 0.4 is needed to produce the best results for mixing application with respect to channel geometry ratio (H/L_c) of 0.25. It also shows that the optimum value of filament length for mixing in micro-devices is critically influenced by channel geometry and bending rigidity.

Table III.
Tabulation of slope of mean angle θ curve for different filament lengths and bending rigidities along with their corresponding filament deformation patterns

Filament length, Len	Bending rigidity, S_{ben}	Filament deformation pattern	Slope of mean angle θ curves, obtained from Figures 31-36
0.4	1×10^{-3} (Rigid)	Retarded	0.474
	1×10^{-4} (Flexible)	Symmetrical sweep	0.216
0.6	1×10^{-3} (Rigid)	Retarded	0.352
	1×10^{-4} (Flexible)	Symmetrical sweep	0.092
0.8	1×10^{-3} (Rigid)	Symmetrical sweep	0.248
	1×10^{-4} (Flexible)	Symmetrical sweep with appreciable bending	0.03
0.8 (SOFPS)	1×10^{-3} (Rigid)	Symmetrical sweep	0.348
	1×10^{-4} (Flexible)	Symmetrical sweep with appreciable bending	0.038

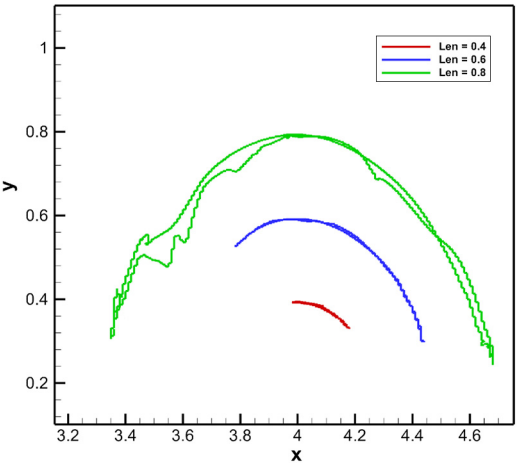

Figure 37.
Trajectory of filament tip with respect to x and y displacement for different filament length, Len = 0.4, 0.6, 0.8 and fixed bending rigidity, $S_{ben} = 1 \times 10^{-3}$ at Reynolds number, Re = 100

3.3 Effect of inlet fluid conditions and bending rigidity on filament deformation

Phase shift in fluid motion has a great impact on filament displacement dynamics, especially for rigid filaments. To obtain a better understanding of filament deformation and bending characteristics for different bending rigidities and fluid flow conditions, we carry out further analysis in which the filament length, Len is fixed to 0.8 spanning three different bending rigidity S_{ben} = 0.01, 0.1 and 1.0. Studies by Lambert and Rangel (2010) had emphasized the importance of analyzing flap dynamics for low Reynolds number ranging from 0.3 to 80. Thus, we consider a fixed Reynolds number of 10.0 for this study. The corresponding filament deformation is analyzed for the two flow conditions keeping a constant value of stretching co-efficient T_{elas} = 10,000. The numerical simulation is carried out for a fixed frequency of oscillation given by St = 0.5. The total simulation time is kept as 3.0. The

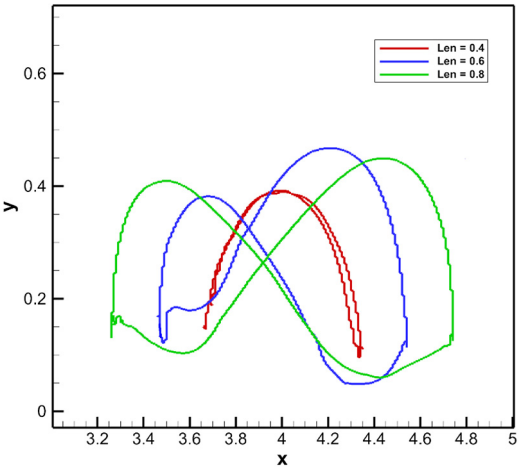

Figure 38.
Trajectory of filament tip with respect to x and y displacement for different filament length, Len = 0.4, 0.6, 0.8 and fixed bending rigidity, $S_{ben} = 1 \times 10^{-4}$ at Reynolds number, Re = 100

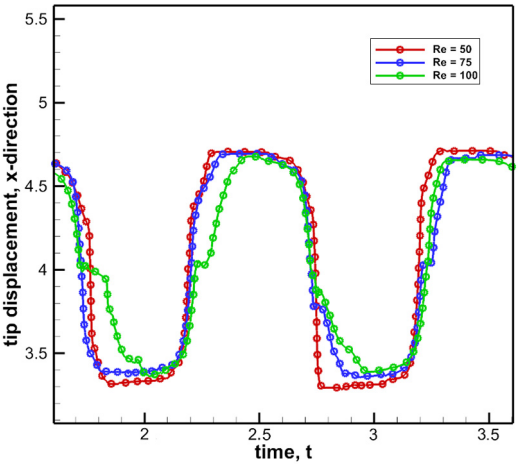

Figure 39.
Filament tip displacement in x-direction with respect to time for different Reynolds numbers, Re = 50, 75, 100 considering fixed filament length, Len = 0.8 and fixed bending rigidity, $S_{ben} = 1 \times 10^{-3}$

filament movement and resulting fluid motion are observed for a time period of 2.0-3.0. The filament positions are captured at fixed time intervals of 0.125. An account of hydrodynamics surrounding the flexible filament is also obtained. The filament deformation and its direction of motion is synonymous with fluid flow direction. In Figure 46, the various positions of the filament are marked by numbers, which indicate the sequence of motion on a sample sinusoidally oscillating fluid flow profile. The nine filament positions can be grouped into two parts i.e. positive fluid cycle and negative cycle. Each cycle can be further divided into forward filament motion and backward filament motion. This is clearly shown in Table IV. The fluid cycle and its corresponding filament motion is applicable to all subsequent cases. The change in fluid and filament directions are observed at Positions 3 and 7.

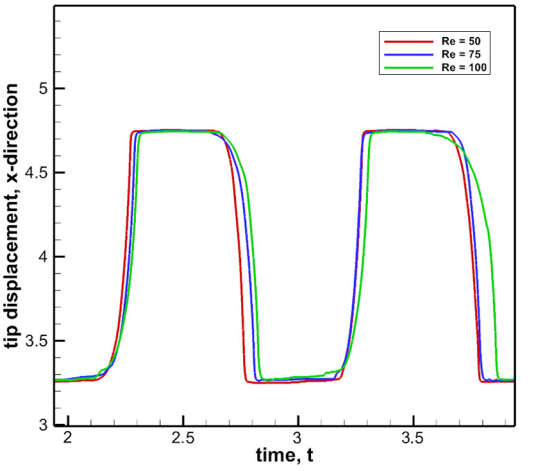

Figure 40.
Filament tip displacement in x-direction with respect to time for different Reynolds numbers, Re = 50, 75, 100 considering fixed filament length, Len = 0.8 and fixed bending rigidity, $S_{ben} = 1 \times 10^{-4}$

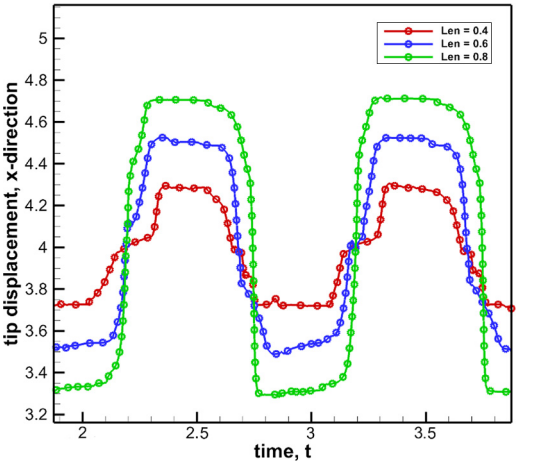

Figure 41.
Filament tip displacement in x-direction with respect to time for different filament length, Len = 0.4, 0.6, 0.8 at Reynolds number, Re = 50 and fixed bending rigidity, $S_{ben} = 1 \times 10^{-3}$

3.3.1 Sinusoidally oscillatory flow with phase shift. The type of pressure-driven fluid flow equation used for the present case is given by equation (23). Three cases of bending rigidity are analyzed, namely, High rigidity (S_{ben} = 1.0), Medium rigidity (S_{ben} = 0.1) and Low rigidity (S_{ben} = 0.01).

3.3.1.1 High rigidity (s_{ben} = 1.0). The motion of the filament in positive x-direction is marked in red and motion in a negative direction is marked in blue. The same convention is applied for all figures. Figure 47 describes the deformation and position of flexible filament for the case of S_{ben} = 1.0. Starting from Position 1 in positive cycle, the filament undergoes a forward motion and steadily elongates with appreciable bending. It reaches maximum extension at Position 3 where the fluid direction changes. Next, the filament returns back to the center of channel at Position 5, thus, completing the positive cycle. A similar extension

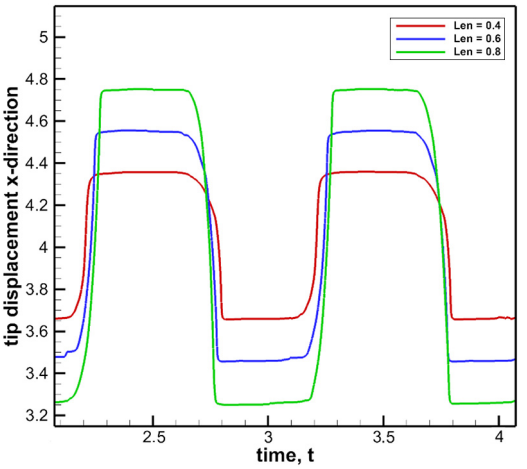

Figure 42. Filament tip displacement in x-direction with respect to time for different filament length, Len = 0.4, 0.6, 0.8 at Reynolds number, Re = 50 and fixed bending rigidity, $S_{ben} = 1 \times 10^{-4}$

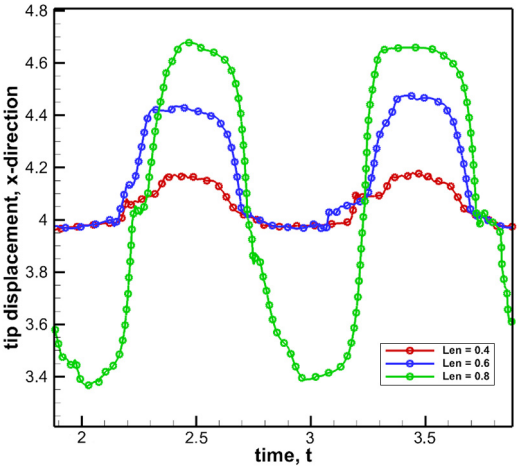

Figure 43. Filament tip displacement in x-direction with respect to time for different filament length, Len = 0.4, 0.6, 0.8 at Reynolds number, Re = 100 and fixed bending rigidity, $S_{ben} = 1 \times 10^{-3}$

and bending occur in a negative cycle with filament changing direction at Position 7 and the negative cycle, thus, concludes at Position 9. Another important observation is that the filament motion in both positive and negative cycle is symmetric. This is an indication of sweeping filament conformity, which is also observed in previous filament deformation studies of Anand *et al.* (2017), thus, making it a good case for fluid mixing applications.

It is clear from the above discussion that the fluid direction changes at Position 3. While the fluid changes direction, a series of streamline images describing the hydrodynamics around the filament is captured. This is shown in Figure 48. The corresponding time is provided with the images. At t = 2.24, the filament is in an elongated position with respect to positive fluid cycle. A recirculation zone is formed near the base of filament. As observed from time t = 2.26 – 2.30, a secondary recirculation zone emerges close to the filament structure and moves from the filament center to tip, gradually increasing in size. The size of the primary zone also increases and at t = 2.30, the secondary zone combines with primary

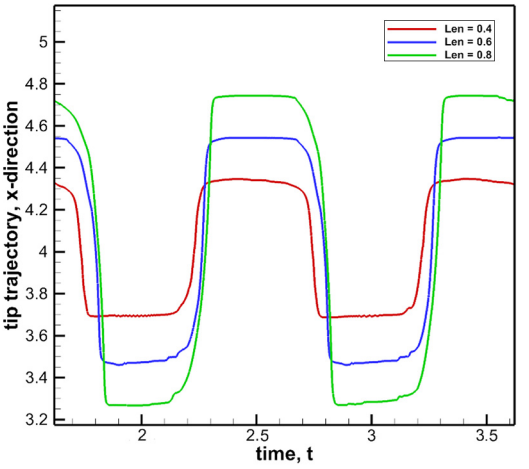

Figure 44.
Filament tip displacement in x-direction with respect to time for different filament length, Len = 0.4, 0.6, 0.8 at Reynolds number, Re = 100 and fixed bending rigidity, $S_{ben} = 1 \times 10^{-4}$

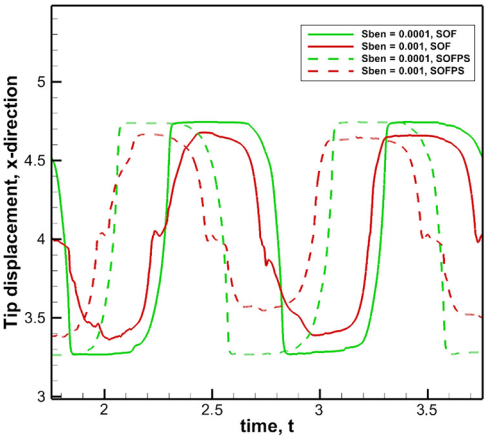

Figure 45.
SOF and SOFPS flow condition comparison of filament tip displacement in x-direction with respect to time at Reynolds number, Re = 100 for fixed filament length, Len = 0.8 and bending rigidities, $S_{ben} = 1 \times 10^{-3}, 1 \times 10^{-4}$

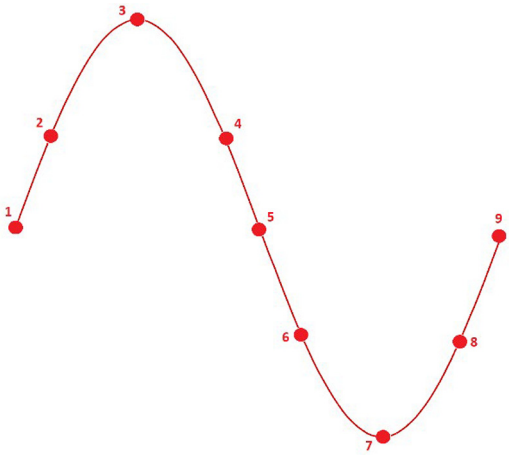

Figure 46.
Various filament positions depicted on a sample profile of oscillating fluid flow

Filament positions	Type of fluid cycle	Type of filament motion	Filament position with respect to initial fluid motion	Filament position with respect to final fluid motion
1-3	Positive	Forward	Position 1	Position 3
3-5	Positive	Backward	Position 3	Position 5
5-7	Negative	Backward	Position 5	Position 7
7-9	Negative	Forward	Position 7	Position 9

Table IV.
Fluid flow direction and its corresponding filament positions

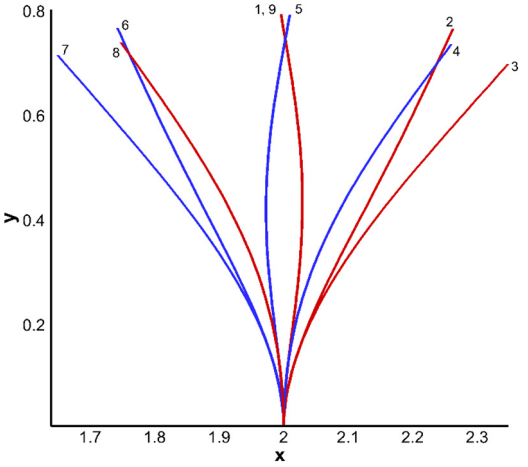

Figure 47.
Instantaneous filament deformation due to SOFPS condition for the case of bending rigidity $S_{ben} = 1.0$ at fixed time interval of 0.125 between time periods 2.0-3.0

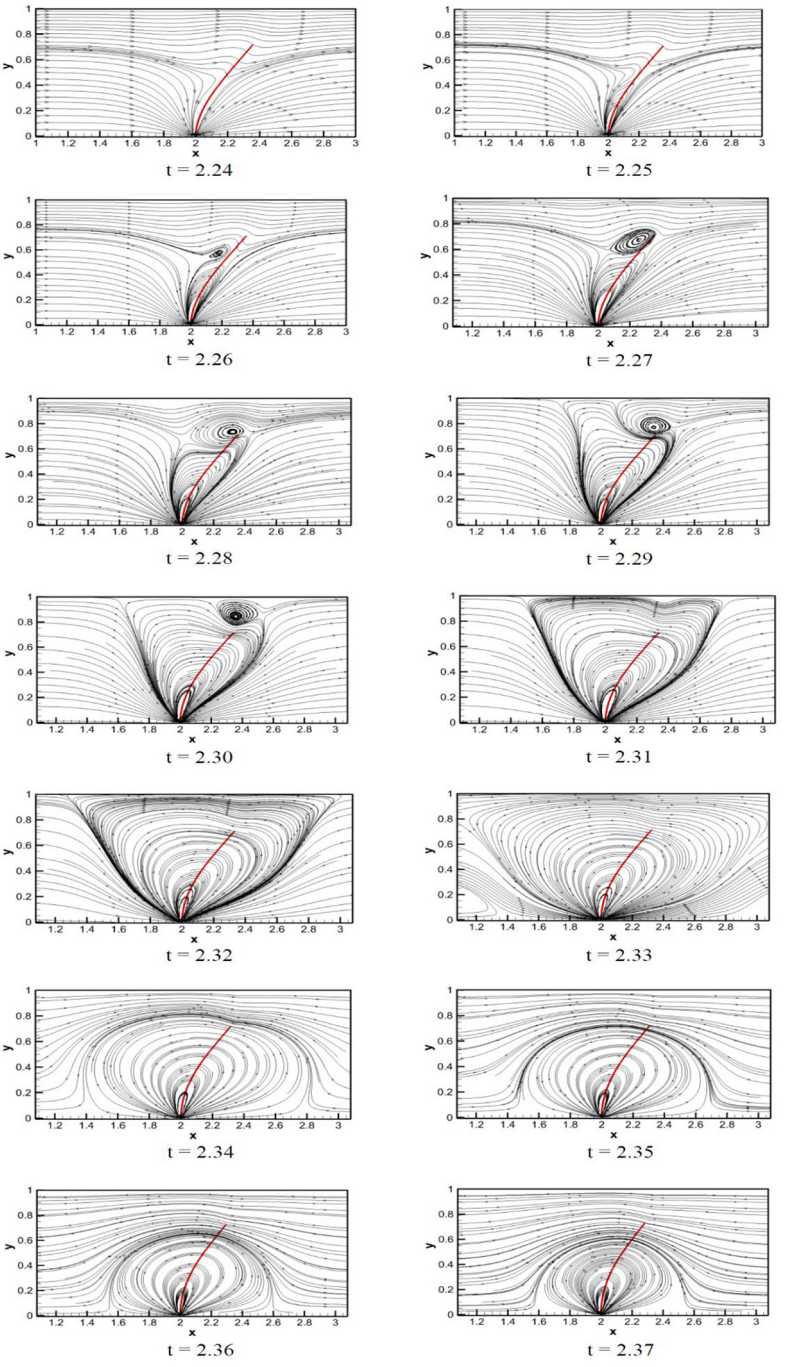

Figure 48.
Streamlines visualization at the vicinity of filament (position 3) at different non-dimensionalized time sequences for S_{ben} = 1.0 during positive fluid cycle

to form a large V-shaped zone around the filament. The V-shaped recirculation zone encompasses a large portion of channel mid-section and reaches maximum size at t = 2.32. At t = 2.33 the fluid velocity reaches a minimum. With the change in fluid direction at t = 2.34, the V-shaped zone shrinks and an oval-shaped zone is formed near the filament base. The size of the ovals shaped zone gradually decreases with time as seen from t = 2.34 to 2.37. The formation of V-shaped zones and subsequent oval-shaped one indicates that fluid molecules near the filament tend to adhere to its surface. First, the filament is high in rigidity, and thus, moves slowly with respect to fluid motion. This prevents the filament to deform considerably and the fluid itself offers high resistance to filament motion. Second, this phenomenon increases mixing efficiency as the fluid is mostly circulating within the large V-shaped zone for case of lower channel geometry ratio. Thus, it is believed that this case can be considered as ideal for fluid mixing.

3.3.1.2 Medium rigidity (s_{ben} = 0.1). The bending rigidity of filament in the present case is S_{ben} = 0.1 and considered to be medium in nature. Figure 49 shows the various filament positions and deformations for SOFPS condition. From Position 1, filament deforms into an arc shape depicted in Position 2. The filament appears to be bent at the center due to lower bending rigidity. Similar arc-shape is also observed in the negative cycle at Position 6. The deformation of filament at Position 4 and 5 are also very similar to that seen in Positions 8 and 1, respectively, but in opposite filament direction. The movement of filament in both positive and negative fluid cycle is thus found to be symmetric in nature.

Figure 50 depicts the series of flow field images captured in the form of streamlines around the flexible filament while the fluid changes direction (Position 3). Similar to the previous case two recirculation zones, one at the base called primary and other at filament center called secondary are formed as seen at time t = 2.25. With an increase in time, the size of both the zones gradually increases. However, the secondary zone grows at a much faster rate compared to the primary. This can be observed for images from t = 2.28 to t = 2.31. The upper half section of the flexible filament has a quick motion when compared to the lower half. Also, the movement of the secondary zone from the center to filament tip is slower than the previous case where filament had bending rigidity S_{ben} = 1.0. The size of the secondary zone reaches a maximum at t = 2.32. Apart from the primary and secondary zones, few other recirculation zones can be observed close to channel edges. Once the fluid reverses direction

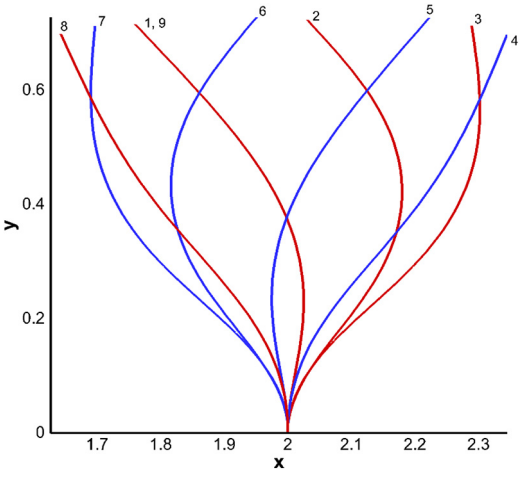

Figure 49. Instantaneous filament deformation due to SOFPS condition for the case of bending rigidity S_{ben} = 0.1 at fixed time interval of 0.125 between time periods 2.0-3.0

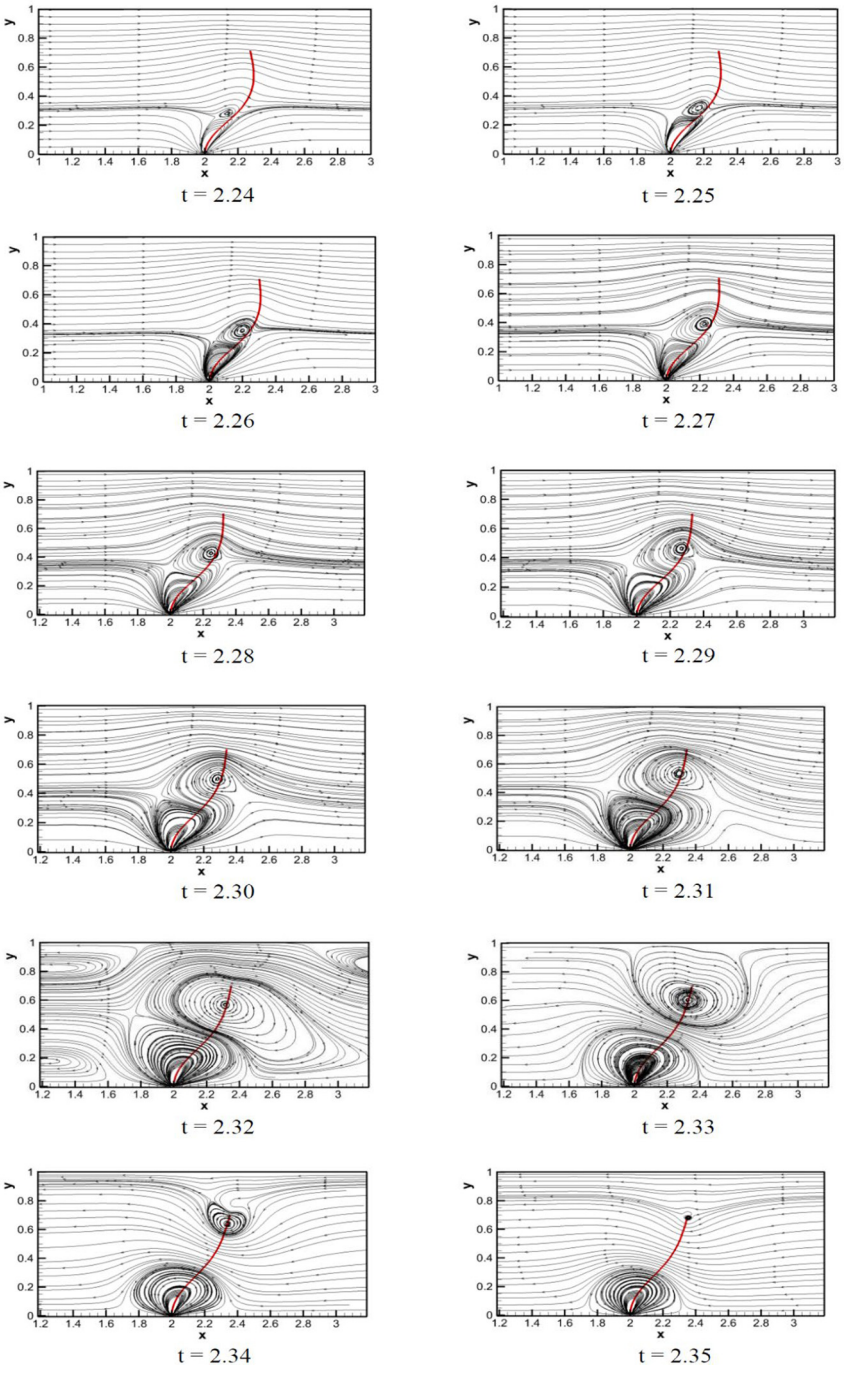

Figure 50.
Streamlines visualization at the vicinity of filament (position 3) at different non-dimensionalized time sequences for S_{ben} = 0.1 during positive fluid cycle

at t = 2.34, the shape of primary zone turns to oval and size of secondary zone gradually diminishes. The secondary zone starts moving toward the tip of filament, and finally, disappears at t = 2.35. Due to the formation of several recirculation zones near channel edges and domination of secondary zone near the filament surface, a good amount of fluid mixing is seen. Fluid entrapment in circulation zones is observed, which also enhances mixing efficiency. Similar types of fluid motion are reported in fluid mixing studies (Lambert and Rangel, 2010).

3.3.1.3 Low rigidity (s_{ben} = 0.01). Similar to previous cases the deformation and positions of filament are recorded for equal time intervals as shown in Figure 51. The filament as observed for Position 1 shows a buckling behavior at the lower half section while the upper half remains straight. This buckling behavior continues with progression of time and is further seen in upper half section at Position 2. The forward motion of the filament in the positive fluid cycle ends with formation of an arc-shaped filament as seen at Position 3. Thus, three different filament shape deformations can be seen for the positive fluid cycle. Similar shape deformation is also observed for the negative fluid cycle. To summarize, a single buckling phenomenon is observed for Positions 1 and 5, multiple filament buckling is seen for Positions 2 and 6. Rest of the filament deformations are of arc-shaped with bending at the center location.

The fluid flow around flexible filament is shown for filament Position 3 in Figure 52. As compared to the previous two cases, the filament bending rigidity is the least. When observing fluid motion for time t = 2.25 – 2.30, the size of primary and secondary recirculation zones as compared that of previous cases are found to be quite small. This indicates that the filament is moving in tandem with fluid flow and is, thereby offering least resistance. At t = 2.31, the size of secondary zone exceeds that of primary. Apart from primary and secondary zone, two other zones are formed near the top left and right channel edges at t = 2.32 during which time the fluid velocity is minimum. The fluid changes direction at t = 2.33, which causes the secondary zone to move slightly away from filament surface. Finally, the secondary zone disappears at t = 2.34. An observation from the above study indicates that the fluid flow around the filament is laminar in nature with small disturbances near the filament structure. The presence of the filament has practically no effect on fluid mixing in the present case.

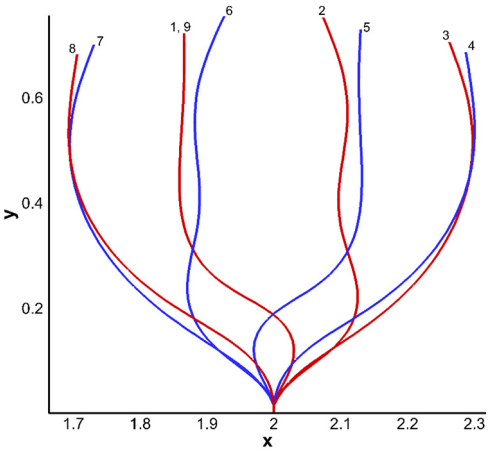

Figure 51. Instantaneous filament deformation due to SOFPS condition for the case of bending rigidity S_{ben} = 0.01 at fixed time interval of 0.125 between time periods 2.0-3.0

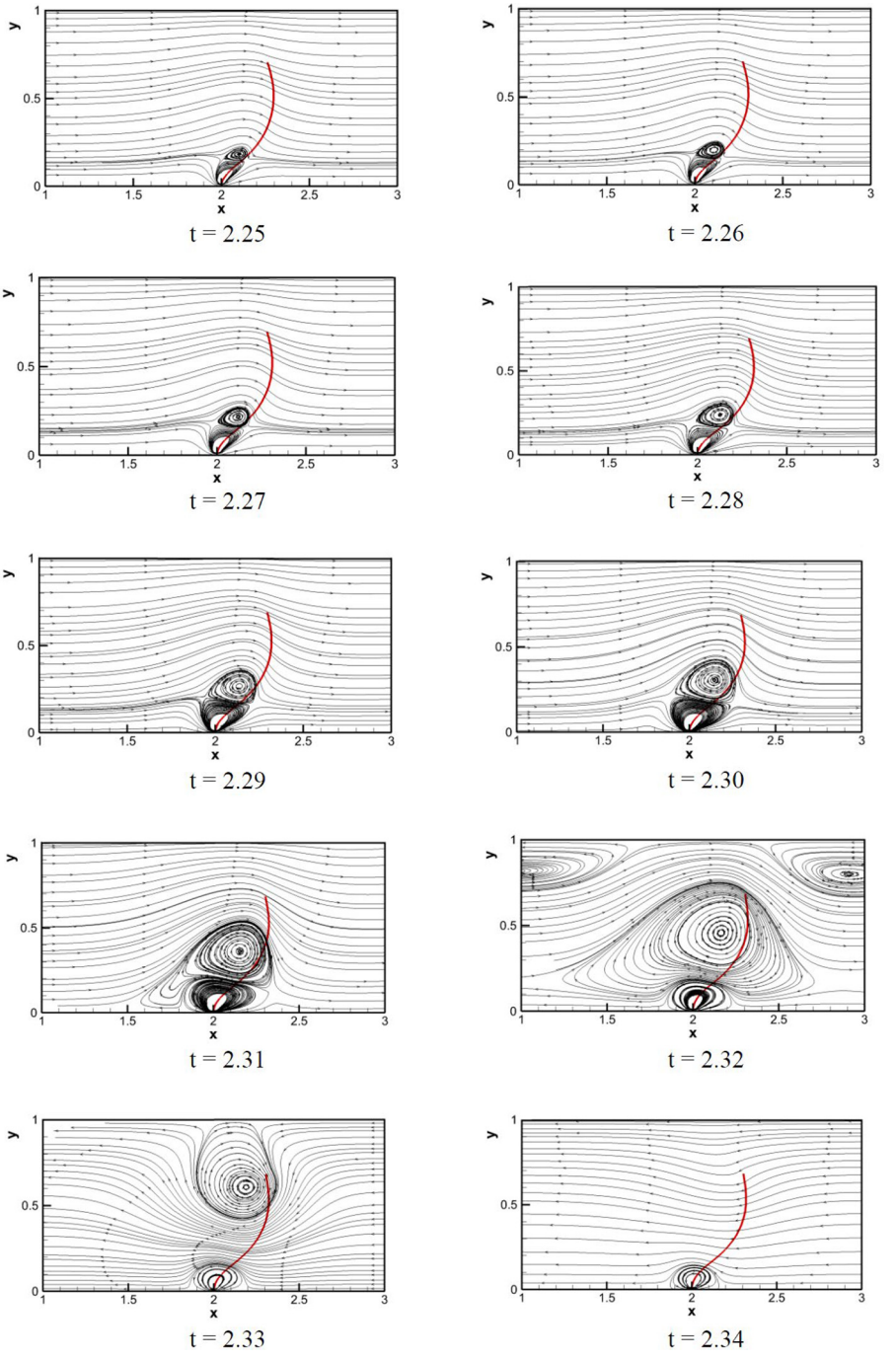

Figure 52.
Streamlines visualization at the vicinity of filament (position 3) at different non-dimensionalized time sequences for S_{ben} = 0.01 during positive fluid cycle

3.3.2 Sinusoidally oscillatory flow without phase shift. The fluid equation governing the flow for the present section is SOF. The corresponding sinusoidal pressure gradient driving the flow is given by equation (24). Similar to SOFPS condition, three cases of bending rigidity are analyzed here, namely, High rigidity (S_{ben} = 1.0), Medium rigidity (S_{ben} = 0.1) and Low rigidity (S_{ben} = 0.01).

3.3.2.1 High rigidity (s_{ben} = 1.0). Figure 53 describes the deformation and position of flexible filament for the case of SOF condition with high rigidity S_{ben} = 1.0. From the figure, a steady elongation coupled with bending is observed for filament Positions 1-3 in the positive fluid cycle. The fluid changes direction at Position 3 and the filament achieve maximum extension in this position. Next, the filament returns back to the center of channel at Position 5, thus, completing the positive cycle. A similar extension and bending occur in a negative cycle with filament changing direction at Position 7 and the negative cycle, thus, concludes at Position 9. An important observation is that the filament motion in both positive and negative cycle is symmetric. The shape deformation seen in the present case is very similar to that observed for SOFPS condition.

3.3.2.2 Medium rigidity (s_{ben} = 0.1). The filament at Position 1 in Figure 54 is almost straight and undergoes bending at the center with passage of time. The positive fluid cycle also produces elongation in filament. When deformations are seen for Positions 4-7 in the backward motion, the filament achieve considerable bending mixed with compression at the center. Finally, the filament returns to its original Position 1 at the end of a fluid negative cycle. Contrary to SOFPS condition, the filament changes direction in a negative cycle at Position 8. A simple observation of filament movement with respect to positions reveal that none of the deformations are similar to each other. Shape replication of filament positions for both positive and negative fluid cycle is not observed. During the forward motion of filament, the fluid is fairly straight, remains elongated and achieves slight bending with time. When looking at the same filament behavior in a backward motion, more pronounced compression and bending is noticed. The filament behaves differently during forward and backward motion. This behavior of filament is very similar to beating cilia and its propulsion mechanism (Barlow *et al.*, 1993; Dauptain *et al.*, 2008). In our study, the filament has no self-propelling feature and is completely passive. It responds to only hydrodynamics stresses acting on its surface. On the other hand, beating cilia produces antiplectic

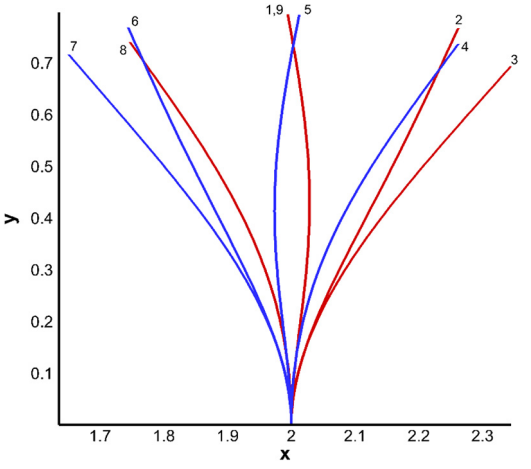

Figure 53. Instantaneous filament deformation due to SOF condition for the case of bending rigidity S_{ben} = 1.0 at fixed time interval of 0.125 between time periods 2.0-3.0

metachronism (Barlow *et al.*, 1993; Dauptain *et al.*, 2008), which creates an oscillating fluid motion responsible for effective stoke. This effective stroke pushes the fluid in the opposite direction, thereby causing the cilia bearing micro-organism to propel further. For the case of SOF condition, the filament behaves in an asymmetric fashion similar to beating cilia. Thus, the present case clearly depicts the form of fluid motion produced during ciliary propulsion.

To further demonstrate that the present case depicts cilia beating, streamlines plots are generated near filament surface for Position 8 as shown in Figure 55. The fluid is moving from right to left in the negative fluid cycle. A primary recirculation zone is formed at the base of filament at t = 2.04. With time, a secondary zone emerges from the upper channel edge while a tertiary zone is created behind the filament. The size of the secondary zone increases in size has more fluid gets entrapped within it. As fluid velocity becomes minimum at t = 2.07, tertiary and secondary zone combine to form large high-velocity zone behind the filament. With change in fluid direction from left to right, the secondary zone is released toward the right in same direction of fluid flow as seen from images t = 2.08 to t = 2.10. This phenomenon is called cross-stream fluid flow, which can be potentially used for micro-pumping applications (Anand *et al.*, 2017). All recirculation zones disappear at t = 2.11. Another important observation is that bending rigidity also plays a critical role in producing the asymmetric beat pattern in filament.

3.3.2.3 Low rigidity (s_{ben} = 0.01). The deformation and filament positions for the case of S_{ben} = 0.01 subjected to SOF condition is given in Figure 56. The filament shows slight buckling at Position 1 and continues to elongate with minimum bending during forward motion. A significant buckling is seen at the lower half of filament at Positions 5 and 6 during backward motion. By keeping x co-ordinate 2 as a reference, the movement of the filament in positive and negative x-direction is analyzed. The movement of the filament is restricted to x co-ordinate 1.8 during negative cycle (Position 7) while filament elongates and moves beyond x co-ordinate 2.6 during positive cycle (Position 3). Thus, a clear asymmetry exists in filament deformation during both fluid cycles. Even though asymmetry exists, the filament positions at fixed intervals of time do not match that of beating cilia. This can also be observed by comparing the filament positions formed during forward and backward motion between the present case and that of medium rigidity S_{ben} = 0.1 case. Fluid flow surrounding flexible filament at Position 8 is provided in Figure 57 in the form of streamlines. The present case has the lowest bending rigidity. Due to this feature, the

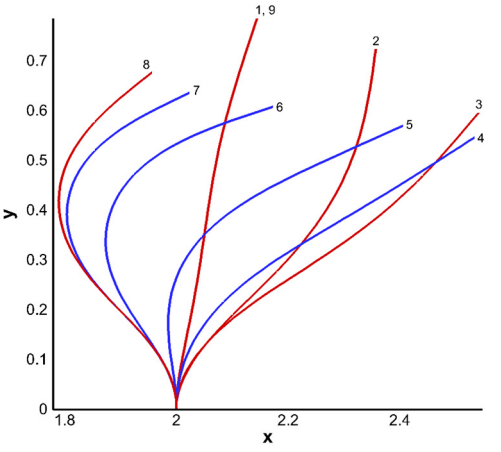

Figure 54.
Instantaneous filament deformation due to SOF condition for the case of bending rigidity S_{ben} = 0.1 at fixed time interval of 0.125 between time periods 2.0-3.0

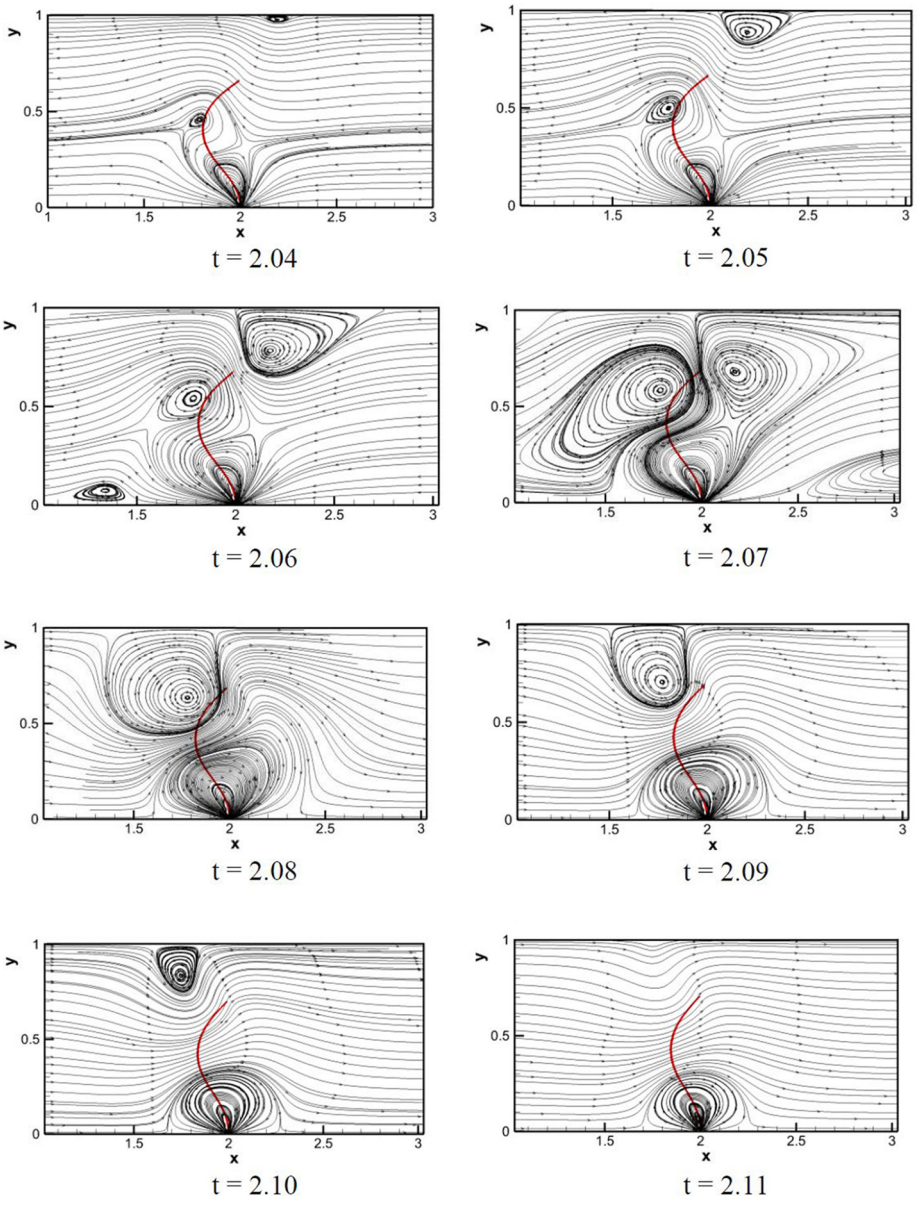

Figure 55. Streamlines visualization at the vicinity of filament (position 8) at different non-dimensionalized time sequences for S_{ben} = 0.1 during negative fluid cycle

filament offers very low resistance to fluid motion. In the location of filament bending, a small recirculation zone is formed as seen at time t = 2.06. Two large zones are observed at t = 2.07. This is the time at which the fluid velocity becomes minimum. With a change in fluid direction (t = 2.08), small zones are created near filament surface, which does not show any significant impact on the surrounding fluid dynamics. The fluid is laminar in nature with small oval-shaped primary zones created near the base as seen at time t = 2.09 and t = 2.10.

3.4 Comparison between sinusoidal oscillatory flow with phase shift and sinusoidal oscillatory flow conditions

In the previous sections, the filament deformation and fluid flow surrounding the filament are analyzed by comparing positions and streamlines for both SOFPS and SOF conditions. In the present section, we correlate this behavior in terms of end-to-end distance (d_{ee}) and tip trajectory for the two flow conditions.

3.4.1 End-to-end distance (d_{ee}). The factor end-to-end distance (d_{ee}) signifies the amount of stretching/compression, bending or buckling produced by the filament. It is defined as the shortest distance between the fixed and free filament ends. The length of the filament is the actual end-to-end distance before the start of the simulation. The filament end-to-end distance (d_{ee}) for the case of high rigidity S_{ben} = 1.0 is shown in Figure 58. A percentage (%) deviation of end-to-end distance with respect to original filament length is tabulated in Table V. Filaments in this group show a considerable amount of stretching and compression. The filament subjected to SOFPS show lower levels of deviation within the first time period compared to SOF condition. From time period one onwards, the level of deviation remains the same for both conditions. A phase shift is observed between filament end-to-end distances due to the two flow conditions. Filament in SOFPS condition has the lowest deviation of 2.5 per cent while SOF condition produces 3.12 per cent. Filaments having high rigidity (S_{ben} = 1.0) and subjected to varying flow conditions produce symmetric behavior in filament deformation. Similar observations are noted when analyzing filament positions in previous sections and the same can be confirmed from Figure 58. The end-to-end distance (d_{ee}) of a filament having medium rigidity (S_{ben} = 0.1) is shown in Figure 59. Filament subjected to both conditions exhibit an initial bending state and remain in the same state throughout the simulation time. Filament placed in SOFPS

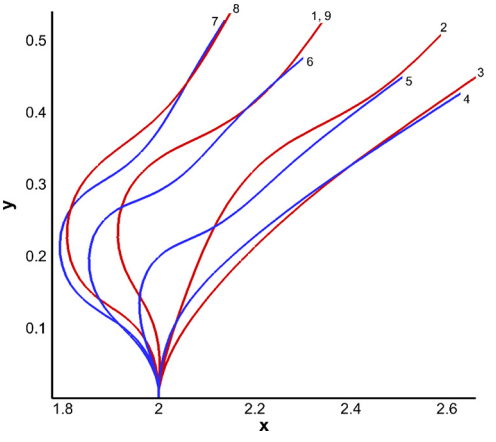

Figure 56.
Instantaneous filament deformation due to SOF condition for the case of bending rigidity S_{ben} = 0.01 at fixed time interval of 0.125 between time periods 2.0-3.0

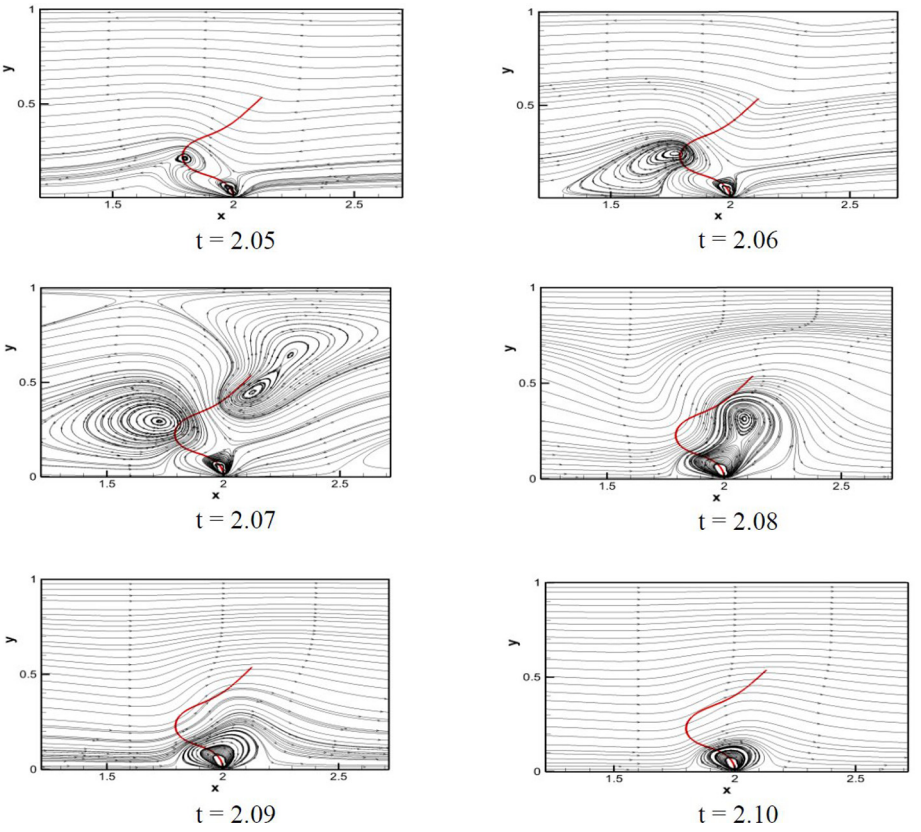

Figure 57. Streamlines visualization at the vicinity of filament (position 8) at different non-dimensionalized time sequences for S_{ben} = 0.01 during negative fluid cycle

condition shows the lowest deviation of 10.6 per cent, whereas filament in SOF condition shows about 30 per cent deviation. The amount of deviation for SOF condition reduces with passage of time while that for SOFPS condition remains almost constant as seen in Figure 59. Finally, Figure 60 shows d_{ee} for filament with lowest rigidity S_{ben} = 0.01. Both flow conditions produce buckling states in filament. The pattern of end-to-end distance plot for SOFPS condition is neither sinusoidal nor uniform in nature when compared to high and medium rigidity cases. This also indicates filament buckling during successive time periods. The lowest deviation obtained for SOFPS condition is 8.75 per cent and that for SOF condition is 33.75 per cent. With an increase in time, the level of deviation keeps on increasing for SOF condition, whereas it remains almost constant for SOFPS condition. The filaments that are subjected to both the flow conditions have three things in common. First, filament having high rigidity (S_{ben} = 1.0), undergo cyclic stretching and compression, second filament having medium rigidity (S_{ben} = 0.1), show successive bending, third filament having low rigidity (S_{ben} = 0.01), undergoes buckling. These observations are obtained from visual inspection and qualitative comparison of filament deformation study carried out in the previous section with end-to-end distance plots in the present section. Thus, we can infer from the above discussion that high rigidity filaments show greater levels of stretching while medium and low rigidity filaments exhibit better bending and buckling, respectively.

Also, filament buckling is seen only in low rigidity filament placed in SOFPS and SOF condition. When comparing end-to-end distances for medium and low rigidity filaments placed in both flow conditions, filaments in SOF condition show significant deviation as seen in Table V. This also indicates asymmetric behavior of medium and low rigidity filaments in SOF condition.

3.4.2 Trajectory of filament tip. The trajectory of the filament tip provides useful information regarding the overall extent of movement of filament structure either in the positive or negative x-direction. As the filament is initially held vertical, the trajectory will begin at x-location 2.0. The symmetric and asymmetry behavior of filament can be analyzed by observing the trajectory in the positive and negative direction. Figure 61 shows the tip trajectory of high rigidity ($S_{ben} = 1.0$) filaments placed in SOFPS and SOF conditions. Except for the first time period, the movement of trajectory in both positive and negative direction is

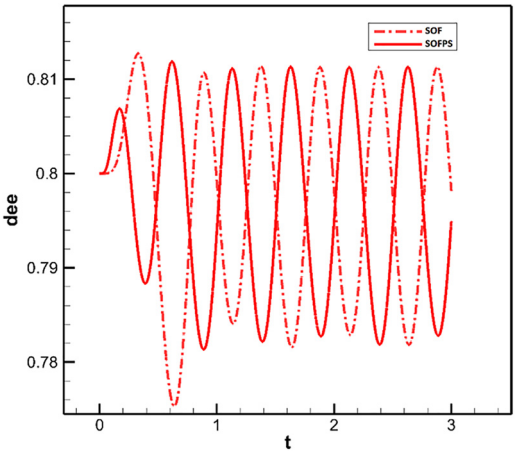

Figure 58.
End-to-end distance (d_{ee}) obtained by filament having high rigidity $S_{ben} = 1.0$ for total simulation time when subjected to SOFPS and SOF conditions

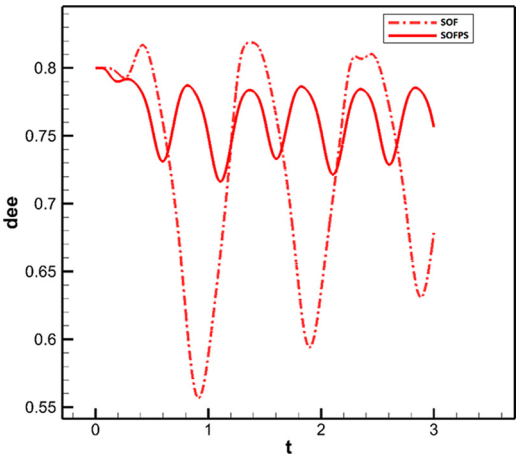

Figure 59.
End-to-end distance (d_{ee}) obtained by filament having medium rigidity $S_{ben} = 0.1$ for total simulation time when subjected to SOFPS and SOF conditions

approximately equal for both flow conditions. The solution attains stability with time, and hence, initial variations in solution are observed for all case studies. Figure 62 provides details of tip trajectory with respect to simulation time for medium rigidity filament. When observing SOFPS condition plot, the trajectory is found to be moving in both a positive and negative direction. The same pattern is seen in Figure 63 for SOFPS condition, which relates filaments of lower rigidity. By analyzing tip trajectory of SOF condition for both medium and lower rigidity filaments, it can be seen that the highest and lowest tip expansions are present only in positive x-direction. The filament tip never enters the negative x-direction region. This is another proof of asymmetry in low and medium rigidity filaments. Thus, it can be inferred that the filament behaves in a symmetric fashion irrespective of bending rigidity when subjected to SOFPS conditions. Also, asymmetric deformation of filament is observed for the ones placed in SOF conditions provided the bending rigidity is medium or lower in nature. It also indicates that filaments that have equispaced sweeping trajectories are well suited for mixing applications while those exhibiting asymmetry behaviors are applicable for fluid pumping.

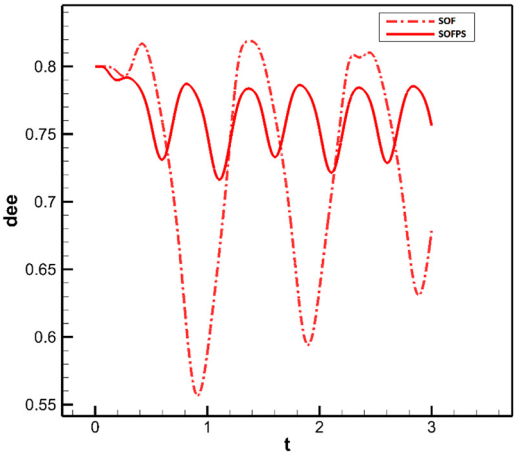

Figure 60.
End-to-end distance (d_{ee}) obtained by filament having low rigidity S_{ben} = 0.01 for total simulation time when subjected to SOFPS and SOF conditions

Table V.
Percentage deviation of filament end-to-end distance for different bending rigidity and flow condition with corresponding filament behavior and deformation observations

Bending rigidity of flexible filament (S_{ben})	Fluid flow conditions with filament behavior		Remarks on corresponding filament deformation
	SOFPS (%)	SOF (%)	
High, 1.0	2.5 (symmetry)	3.12 (symmetry)	Stretching/compression
Medium, 0.1	10.6 (symmetry)	30 (asymmetry)	Bending
Low, 0.01	8.75 (symmetry)	33.75 (asymmetry)	Buckling

4. Conclusion

The primary goal of this study is to understand the fluid-structure interaction of a tethered flexible filament subjected to oscillating fluid flow in a two-dimensional channel. Mechanical properties of the flexible filament such as stretching and bending are incorporated into the governing fluid equations using a temporal second-order IBM. The capability of the developed numerical model to capture the interaction of flexible filaments in oscillating fluid flow as compared to previous research works in the same field is clearly demonstrated. Parametric analysis is first carried out to study the interplay of hydrodynamic stresses acting on the filament surface for different filament length, bending rigidity, flow conditions and Reynolds number. The impact on fluid motion due to an increase in filament length is greater in the longitudinal direction as compared to transverse direction. Longer rigid filaments have a more pronounced influence in a fluid motion for both longitudinal and transverse direction as compared to short flexible filaments. Flexible filaments of all lengths

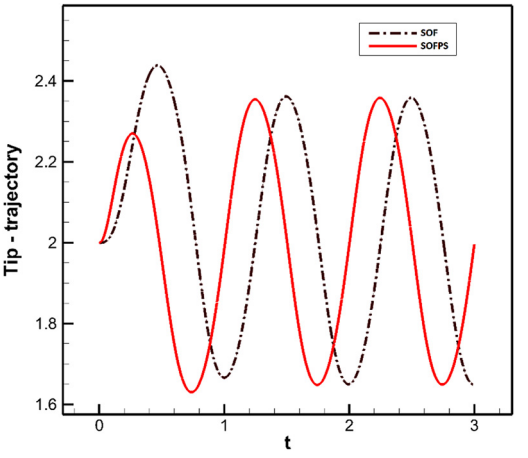

Figure 61.
Trajectory of filament tip when subjected to SOFPS and SOF conditions over total simulation time 3.0 for high rigidity $S_{ben} = 1.0$

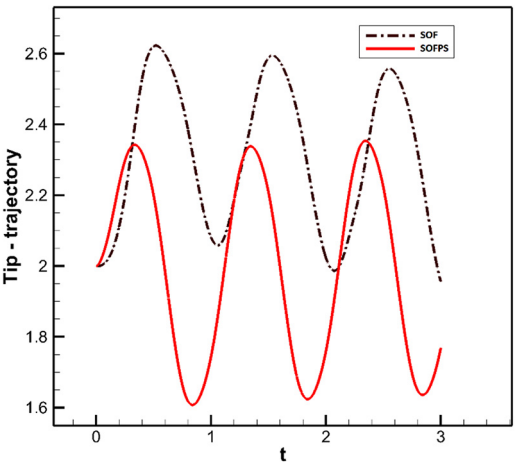

Figure 62.
Trajectory of filament tip when subjected to SOFPS and SOF conditions over total simulation time 3.0 for medium rigidity $S_{ben} = 0.1$

have similar sweeping span, whereas the flapping span for rigid filaments keep increasing as length increases. It is also observed that the sweep span of rigid filament keeps decreasing as Reynolds number increases, whereas in flexible filament case, the sweep span remains constant irrespective of changing Reynolds number. Filaments producing symmetrical sweep pattern were found to produce better mixing, which is in agreement with previous similar studies. On analyzing the angle made by the filament with respect to horizontal, we see that filament producing symmetrical sweep pattern has a slope of mean angle Θ curve value ranging between 0.09 and 0.35. The slope of mean angle Θ curve values existing outside this range produces either a retarded deformation or filament sweep with appreciable bend both of which are not ideal conditions for fluid mixing. The tip trajectories for filament length, Len = 0.6 and 0.8 results in formation of octave-shaped pattern similar to tip motion of beating cilia. The size of the pattern increases with filament length providing an indication of filament bending observed during deformation. A flattened behavior in tip displacement is observed for all cases, which indicates that filament remains aligned in the fluid flow direction. There is also greater retardation of filament displacement for rigid lower length filaments as Reynolds number increases. Retarded motion is observed for rigid filaments of length, Len = 0.4 and Len = 0.6, whereas sweep with an appreciable bend is seen for flexible filament of length, Len = 0.8. This clearly shows that selection of right filament length and bending rigidity is crucial for fluid mixing scenarios. The phase shift in fluid motion is also found to critically effect filament displacement dynamics, especially for rigid filaments. We also found that aspect ratio i.e. ratio of filament length to channel height, suitable for mixing applications is directly dependent on channel geometry ratio i.e. ratio of channel height to channel length. It is clear that a minimum aspect ratio (Len/H) of 0.4 is needed to produce the best results for mixing application with respect to channel geometry ratio (H/L_c) of 0.25.

On the basis of the parametric analysis done, we studied filament displacement and corresponding flow streams for two types of flow variations i.e. SOFPS and SOF for rigid filament cases S_{ben} = 0.01, 0.1 and 1.0 referred to as low, medium and high rigidity filaments. Presence of the filament and its interaction with these flow conditions produce complex filament deformations. The motion and fluid flow surrounding the filament are well captured for fixed time intervals throughout the simulation. Filaments having high and

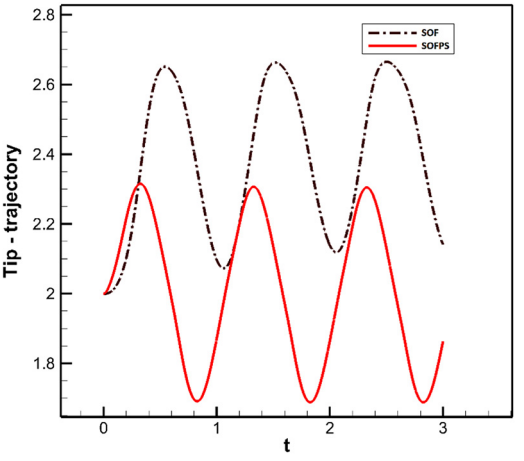

Figure 63.
Trajectory of filament tip when subjected to SOFPS and SOF conditions over total simulation time 3.0 for low rigidity S_{ben} = 0.01

medium rigidity, show pronounced levels of elongation or stretching and have lower levels of bending. This results in sweeping filament conformation ideal for fluid mixing. Also, their filament deformations are symmetric in nature irrespective of flow conditions. Symmetric behaviors are also seen for medium and low rigidity filament subjected to SOFPS condition. However, filament deform asymmetrically for SOF condition. Filaments belonging to the same medium rigidity category but when placed in SOF condition produce a phenomenon similar to antiplectic metachronism. Another observation is that filament show high levels of buckling when the bending rigidity is low.

The present study involves passive tethered filament moving with respect to an oscillating fluid flow whose flow conditions (SOFPS and SOF) are assumed beforehand. However, actively propelling filaments surrounded by stationary fluid, deform in specific ways, which are highly acceptable for engineering applications such as fluid mixing or micro-pumping. It is possible in the present study to perfectly match these filament deformations with results obtained from assumed flow conditions, thereby indirectly defining the flow behavior for the above-mentioned practical engineering applications. Symmetric filament behavior is adequate for mixing scenarios while asymmetric behavior is favorable for pumping. Thus, the above observations can be concluded with two key findings:

(1) Effective fluid mixing can be enabled in devices, which consist of high and medium rigidity filaments that deform to produce SOFPS in an oscillating sequence.

(2) Pumping in micro-devices can be attained by the use of medium rigidity filaments that deform to create SOF condition in the surrounding fluid.

References

Adeeb, E., Haider, B.A. and Sohn, C.H. (2018), "Influence of rounded corners on flow interference between two tandem cylinders using FVM and IB-LBM", *International Journal of Numerical Methods for Heat and Fluid Flow*, Vol. 28 No. 7, pp. 1648-1663.

Alexeev, A., Yeomans, J.M. and Balazs, A.C. (2008), "Designing synthetic, pumping cilia that switch the flow direction in microchannels", *Langmuir*, Vol. 24 No. 21, pp. 12102-12106.

Anand, D.V., Patnaik, B.S.V. and Vedantam, S. (2017), "A dissipative particle dynamics study of a flexible filament in confined shear flow", *Soft Matter*, Vol. 13 No. 7, pp. 1472-1480.

Ardekani, A.M., Dabiri, S. and Rangel, R.H. (2008), "Collision of multi-particle and general shape objects in a viscous fluid", *Journal of Computational Physics*, Vol. 227 No. 24, pp. 10094-10107.

Baaijens, F.P. (2001), "A fictitious domain/mortar element method for fluid–structure interaction", *International Journal for Numerical Methods in Fluids*, Vol. 35 No. 7, pp. 743-761.

Bamiro, O.O. and Liou, W.W. (2013), "A direct heating immersed boundary-lattice boltzmann method for thermal flows", *International Journal of Numerical Methods for Heat and Fluid Flow*, Vol. 24 No. 1, pp. 169-200.

Barlow, D.A.V.I.D., Sleigh, M.A. and White, R.J. (1993), "Water flows around the comb plates of the ctenophore pleurobrachia plotted by computer: a model system for studying propulsion by antiplectic metachronism", *Journal of Experimental Biology*, Vol. 177 No. 1, pp. 113-128.

Connell, B.S. and Yue, D.K. (2007), "Flapping dynamics of a flag in a uniform stream", *Journal of Fluid Mechanics*, Vol. 581, pp. 33-67.

Dauptain, A., Favier, J. and Bottaro, A. (2008), "Hydrodynamics of ciliary propulsion", *Journal of Fluids and Structures*, Vol. 24 No. 8, pp. 1156-1165.

De Marinis, D., de Tullio, M.D., Napolitano, M. and Pascazio, G. (2016), "Improving a conjugate-heat-transfer immersed-boundary method", *International Journal of Numerical Methods for Heat and Fluid Flow*, Vol. 26 Nos 3/4, pp. 1272-1288.

Diaz-Goano, C., Minev, P.D. and Nandakumar, K. (2003), "A fictitious domain/finite element method for particulate flows", *Journal of Computational Physics*, Vol. 192 No. 1, pp. 105-123.

Farnell, D.J.J., David, T. and Barton, D.C. (2004), "Numerical simulations of a filament in a flowing soap film", *International Journal for Numerical Methods in Fluids*, Vol. 44 No. 3, pp. 313-330.

Francois, M., Uzgoren, E., Jackson, J. and Shyy, W. (2004), "Multigrid computations with the immersed boundary technique for multiphase flows", *International Journal of Numerical Methods for Heat and Fluid Flow*, Vol. 14 No. 1, pp. 98-115.

Griffith, B.E., Luo, X., McQueen, D.M. and Peskin, C.S. (2009), "Simulating the fluid dynamics of natural and prosthetic heart valves using the immersed boundary method", *International Journal of Applied Mechanics*, Vol. 1 No. 1, pp. 137-177.

Hayase, T., Humphrey, J.A.C. and Greif, R. (1992), "A consistently formulated QUICK scheme for fast and stable convergence using finite-volume iterative calculation procedures", *Journal of Computational Physics*, Vol. 98 No. 1, pp. 108-118.

Hu, H.H., Patankar, N.A. and Zhu, M.Y. (2001), "Direct numerical simulations of fluid–solid systems using the arbitrary lagrangian–eulerian technique", *Journal of Computational Physics*, Vol. 169 No. 2, pp. 427-462.

Hua, H., Shin, J. and Kim, J. (2014), "Dynamics of a compound droplet in shear flow", *International Journal of Heat and Fluid Flow*, Vol. 50, pp. 63-71.

Huang, W.X., Chang, C.B. and Sung, H.J. (2012), "Three-dimensional simulation of elastic capsules in shear flow by the penalty immersed boundary method", *Journal of Computational Physics*, Vol. 231 No. 8, pp. 3340-3364.

Huang, W.X., Shin, S.J. and Sung, H.J. (2007), "Simulation of flexible filaments in a uniform flow by the immersed boundary method", *Journal of Computational Physics*, Vol. 226 No. 2, pp. 2206-2228.

Huang, W.X. and Sung, H.J. (2009), "An immersed boundary method for fluid–flexible structure interaction", *Computer Methods in Applied Mechanics and Engineering*, Vol. 198 Nos 33/36, pp. 2650-2661.

Huang, W.X. and Sung, H.J. (2010), "Three-dimensional simulation of a flapping flag in a uniform flow", *Journal of Fluid Mechanics*, Vol. 653, pp. 301-336.

Kanchan, M. and Maniyeri, R. (2019), "Numerical analysis of the buckling and recuperation dynamics of flexible filament using an immersed boundary framework", *International Journal of Heat and Fluid Flow*, Vol. 77, pp. 256-277.

Khatavkar, V.V., Anderson, P.D., den Toonder, J.M. and Meijer, H.E. (2007), "Active micromixer based on artificial cilia", *Physics of Fluids*, Vol. 19 No. 8, p. 083605.

Kim, B., Chang, C.B., Park, S.G. and Sung, H.J. (2015), "Inertial migration of a 3D elastic capsule in a plane poiseuille flow", *International Journal of Heat and Fluid Flow*, Vol. 54, pp. 87-96.

Kim, B., Park, S.G., Huang, W. and Sung, H.J. (2016), "Self-propelled heaving and pitching flexible fin in a quiescent flow", *International Journal of Heat and Fluid Flow*, Vol. 62, pp. 273-281.

Kim, B., Park, S.G., Huang, W.X. and Sung, H.J. (2017), "An autonomous flexible propulsor in a quiescent flow", *International Journal of Heat and Fluid Flow*, Vol. 68, pp. 151-157.

Kim, Y. and Peskin, C.S. (2006), "2-D parachute simulation by the immersed boundary method", *SIAM Journal on Scientific Computing*, Vol. 28 No. 6, pp. 2294-2312.

Kim, Y. and Peskin, C.S. (2007), "Penalty immersed boundary method for an elastic boundary with mass", *Physics of Fluids*, Vol. 19 No. 5, p. 053103.

Kim, Y. and Peskin, C.S. (2009), "3-D parachute simulation by the immersed boundary method", *Computers and Fluids*, Vol. 38 No. 6, pp. 1080-1090.

Krafczyk, M., Tölke, J., Rank, E. and Schulz, M. (2001), "Two-dimensional simulation of fluid–structure interaction using lattice-Boltzmann methods", *Computers and Structures*, Vol. 79 No. 22-25, pp. 2031-2037.

Ladd, A.J. (1994), "Numerical simulations of particulate suspensions via a discretized boltzmann equation. Part 1. Theoretical foundation", *Journal of Fluid Mechanics*, Vol. 271, pp. 285-309.

Lai, M.C. and Peskin, C.S. (2000), "An immersed boundary method with formal second-order accuracy and reduced numerical viscosity", *Journal of Computational Physics*, Vol. 160 No. 2, pp. 705-719.

Lallemand, P. and Luo, L.S. (2003), "Lattice boltzmann method for moving boundaries", *Journal of Computational Physics*, Vol. 184 No. 2, pp. 406-421.

Lambert, R.A. and Rangel, R.H. (2010), "The role of elastic flap deformation on fluid mixing in a microchannel", *Physics of Fluids*, Vol. 22 No. 5, p. 052003.

Li, Y., Li, D., Bie, S., Wang, Z., Zhang, H., Tang, X. and Zhen, Z. (2018), "Numerical simulation for fluid droplet impact on discrete particles with coupled SPH-DEM method", *International Journal of Numerical Methods for Heat and Fluid Flow*, Vol. 28 No. 11, pp. 2581-2605.

Maniyeri, R. and Kang, S. (2014a), "Hydrodynamic interaction between two swimming bacterial flagella in a viscous fluid – a numerical study using an immersed boundary method", *Progress in Computational Fluid Dynamics, an International Journal*, Vol. 14 No. 6, pp. 375-385.

Maniyeri, R. and Kang, S. (2014b), "Numerical study on bacterial flagellar bundling and tumbling in a viscous fluid using an immersed boundary method", *Applied Mathematical Modelling*, Vol. 38 No. 14, pp. 3567-3590.

Maniyeri, R., Suh, Y.K., Kang, S. and Kim, M.J. (2012), "Numerical study on the propulsion of a bacterial flagellum in a viscous fluid using an immersed boundary method", *Computers and Fluids*, Vol. 62, pp. 13-24.

Park, S.G., Chang, C.B., Huang, W.X. and Sung, H.J. (2014), "Simulation of swimming oblate jellyfish with a paddling-based locomotion", *Journal of Fluid Mechanics*, Vol. 748, pp. 731-755.

Park, S.G., Kim, B., Lee, J., Huang, W.X. and Sung, H.J. (2015), "Dynamics of prolate jellyfish with a jet-based locomotion", *Journal of Fluids and Structures*, Vol. 57, pp. 331-343.

Peskin, C.S. (1972), "Flow patterns around heart valves: a numerical method", *Journal of Computational Physics*, Vol. 10 No. 2, pp. 252-271.

Peskin, C.S. (2002), "The immersed boundary method", *Acta Numerica*, Vol. 11, pp. 479-517.

Qin, F.H., Huang, W.X. and Sung, H.J. (2012), "Simulation of small swimmer motions driven by tail/flagellum beating", *Computers and Fluids*, Vol. 55, pp. 109-117.

Rejniak, K.A. and Dillon, R.H. (2007), "A single cell-based model of the ductal tumour microarchitecture", *Computational and Mathematical Methods in Medicine*, Vol. 8 No. 1, pp. 51-69.

Ryu, J., Park, S.G. and Sung, H.J. (2018), "Flapping dynamics of inverted flags in a side-by-side arrangement", *International Journal of Heat and Fluid Flow*, Vol. 70, pp. 131-140.

Santarelli, C., Kempe, T. and Fröhlich, J. (2016), "Immersed boundary methods for heat transfer", *International Journal of Numerical Methods for Heat and Fluid Flow*, Vol. 26 No. 2, pp. 504-514.

Shin, S.J., Chang, C.B. and Sung, H.J. (2012), "Simulation of a valveless pump with an elastic tube", *International Journal of Heat and Fluid Flow*, Vol. 38, pp. 13-23.

Shin, S.J. and Sung, H.J. (2010), "Three-dimensional simulation of a valveless pump", *International Journal of Heat and Fluid Flow*, Vol. 31 No. 5, pp. 942-951.

Shin, S.J. and Sung, H.J. (2012), "Dynamics of an elastic capsule in moderate Reynolds number poiseuille flow", *International Journal of Heat and Fluid Flow*, Vol. 36, pp. 167-177.

Shu, C., Ren, W.W. and Yang, W.M. (2013), "Novel immersed boundary methods for thermal flow problems", *International Journal of Numerical Methods for Heat and Fluid Flow*, Vol. 23 No. 1, pp. 124-142.

Ulrike, K.M. (2003), "Fish'n flag", *Science*, Vol. 302, pp. 1511-1512.

Xia, G. and Lin, C.L. (2008), "An unstructured finite volume approach for structural dynamics in response to fluid motions", *Computers and Structures*, Vol. 86 Nos 7/8, pp. 684-701.

Yu, Z. (2005), "A DLM/FD method for fluid/flexible-body interactions", *Journal of Computational Physics*, Vol. 207 No. 1, pp. 1-27.

Zhang, L.T. and Gay, M. (2007), "Immersed finite element method for fluid-structure interactions", *Journal of Fluids and Structures*, Vol. 23 No. 6, pp. 839-857.

Zhu, L. and Peskin, C.S. (2002), "Simulation of a flapping flexible filament in a flowing soap film by the immersed boundary method", *Journal of Computational Physics*, Vol. 179 No. 2, pp. 452-468.

Corresponding author
Ranjith Maniyeri can be contacted at: mranji1@nitk.edu.in